



Title	Theorization on ion-exchange equilibria: activity of species in 2-D phases.
Author(s)	Tamura, Hiroki
Citation	Journal of Colloid and Interface Science, 279(1), 1-22 <a href="https://doi.org/10.1016/j.jcis.2004.07.010">https://doi.org/10.1016/j.jcis.2004.07.010</a>
Issue Date	2004-11-01
Doc URL	<a href="http://hdl.handle.net/2115/14604">http://hdl.handle.net/2115/14604</a>
Type	article (author version)
File Information	JCIS2004-279-1.pdf



[Instructions for use](#)

**Theorization on Ion-Exchange Equilibria**  
**-Activity of Species in 2-D Phases-**

Hiroki Tamura

Laboratory of Materials Chemistry  
Graduate School of Engineering  
Hokkaido University  
Sapporo, 060-8628 Japan

\*Corresponding author

Hiroki Tamura  
Laboratory of Materials Chemistry  
Graduate School of Engineering  
Hokkaido University, Sapporo, 060-8628 Japan  
Tel: +81-11-706-6741; Fax: +81-11-706-6740  
Email: h-tamura@eng.hokudai.ac.jp

## Abstract

Ion-exchange reactions are naturally occurring at soil and sediment/water interphases, determining soil fertility and water quality. These ion-exchange reactions with inorganic and organic exchangers are applied to chemical analysis, recovery of useful ions from low grade ores (potentially from sea water), water purification including the preparation of "ultra-pure" water, production of foods and medicines, therapy, and others. It is important to theorize about or to model ion-exchange reactions for quantitative explanations of ion-exchange phenomena and for efficient operation of ion-exchange processes. This paper describes the modeling of ion-exchange *equilibria for hydroxyl sites on metal oxides and carboxyl sites in resins with monovalent cations (alkali metal ions), a monovalent anion (nitrate ion), and divalent heavy metal ions.*

The procedure of modeling is as follows: the stoichiometry and material balance equations of the respective ion-exchange reactions were established based on findings here and by others. The equilibrium conditions were given by the Frumkin equation where the mass-action relation is modified with lateral interactions between species at the interphase. The model equations were fitted to the measured data and model parameter values were determined by nonlinear regression analysis. The formation of bonds between ions and exchanger sites was evaluated by the equilibrium constant and the suppression of bond formation by electrostatic, geometric, and other lateral interactions was evaluated by the interaction constant.

It was *established* that the properties of ions are determined by the valence, size, and hydration state of the ions. Monovalent ions (anions and cations) react with oxide surface hydroxyl and resin carboxyl sites as hydrated ions *and* form loose ion-site pairs by a weak electrostatic bond (nonspecific adsorption). However, *the* lateral interactions are large because of a large polarization of the ion-site pairs. When the monovalent cations are dehydrated to react with carboxyl sites in narrow resin nanopores, the bond formation is difficult because energy for dehydration is necessary. The suppressive lateral interactions *here* are small because *of* a small polarization of the dehydrated ion-site pairs that are in direct contact. Divalent heavy metal ions react with oxide hydroxyl sites

by replacing their hydrated water molecules and form ion-site pairs in direct strong contact (specific adsorption). The bond formation becomes easier with increasing charge density of the ions evaluated by the charge/radius ratio, agreeing with the order of these ions to form hydroxo complexes in solution. The suppressive lateral interaction is however small for ions with large charge densities, because a strong contact bond reduces the polarization of ion-site pairs by neutralization.

The properties of exchangers are functions of the molecular and pore environments around the functional groups. The acid-base nature of oxide surface-hydroxyl groups is determined by the electronegativity of surrounding lattice metal ions, and that of resin carboxyl groups by the electron repelling effect of adjacent methyl groups. Pores in oxides have diameters sufficient to accommodate hydrated ions, and the suppression is large because of repulsion from ions adsorbed on opposite pore walls (across-pore interaction). Pores in resins differentiate ions that can access or not access sites on the internal surfaces of the pores. Narrow nanopores with diameters less than those of the hydrated ions require ions to dehydrate before they can enter. The ion-exchange reactivity here is small as described above for dehydrated monovalent ions. In wide nanopores where hydrated ions can enter, the bond formation is easier, but the suppression is larger because of a larger polarization of hydrated ion-site pairs and also of the across-pore interaction. Macropores have diameters much larger than those of the hydrated ions and the bond formation is the same as that in wide nanopores, but the suppression is smaller because of the absence of the across-pore interaction.

Finally, this paper attempts a formulation of activity coefficients of exchanging sites and adsorbed ion-site pairs, and compares the proposed activity coefficients of interphase species with that of solution species given by the Debye-Hückel equation.

**Keywords:** metal oxide, weak acid cation-exchange resin, surface hydroxyl group, carboxyl group, ion, ion-exchange reaction, Frumkin equation

## 1. INTRODUCTION

Ion-exchange reactions are related to many processes both in nature and industry. The retention of nutrient salts by soil is an agricultural process for which scientific descriptions of ion-exchange phenomena were first made; here it was found that ammonium ions are adsorbed on soil by releasing calcium and other cations to maintain electric neutrality (1). The pollution of soil with hazardous ions from waste is also due to ion-exchange adsorption, and the ion-concentration levels of natural waters are affected by the extent of such reactions. In ceramics processing, the coagulation and dispersion of raw material powders are controlled by particle surface-charges resulted from ion-exchange reactions. In medical applications, controlled, slow drug delivery has been achieved by using the release of adsorbed drugs from ion exchangers. In the production of antibiotics and vitamins, separation and purification are made with ion exchange resins. The recovery of useful metals from low grade ores, the removal of toxic ions from waste waters, and the production of "ultra-pure" water for washing semiconductor wafers, micromachines, and other fine materials are typical examples of industrial applications of ion exchange. In ion-exchange chromatography, ions are separated from a mixture with ion-exchange resins and determined individually.

For a quantitative interpretation and efficient operation of ion-exchange processes, it is necessary to be able to understand and predict the extent of reactions under given conditions. A mathematical model makes it possible to calculate the extent of the reaction, and the results of calculations serve to select the most effective adsorbents for particular ions and to optimize solution pH, dose of adsorbents, and other conditions. Such models can be used to develop and design ion exchange technologies, and theorization of ion exchange processes is important.

The exchange of ions between a solid exchanger and an external solution phase is relatively rapid, and equilibrium quantities have been measured and used to evaluate the affinities and abilities of exchangers and ions. However, caution must be shown in characterizing ion-exchange properties with measured raw adsorption data because such data strongly depend on the

experimental conditions. For example, at ion concentrations saturating exchange sites, the amounts of ions adsorbed on an exchanger are limited by the capacity of the exchanger and the amounts may be similar irrespective of the kind of ion; while at low concentrations and at low surface coverages with many sites available, the amounts will be different according to the different affinities of ions. To evaluate the properties of ions and exchangers, it is necessary to establish a universal measure by processing raw adsorption data.

In analytical chemistry, thermodynamical equilibrium conditions are well described by the mass-action law for the acid-base, complexation, redox, solvent extraction, and precipitation-dissolution reactions. The equilibrium constant expresses the activity of a certain species when the activities of the other species participating in the reaction are set to unity, and it serves as a universal measure of the properties of the species. Also, with the equilibrium constants, titration curves, the distribution of chemical species in solution, chromatograms, solubilities of precipitates, and other analytical quantities can be calculated for specified conditions. With such calculations, the accuracy of the analysis, the optimum analytical conditions, suitable indicators, the efficiency of separation, and other parameters can be assessed theoretically, and the results help facilitate the design of analytical methods.

For ion-exchange reactions, the equilibrium constant would also serve as a universal measure to evaluate the properties of ions and exchangers, and the concentration ratios in the form of the mass-action law or the selectivity coefficients have often been used. However, they are generally not constant over wide ranges of ion concentrations and surface coverages as pointed out by Kinniburgh et al. (2). This indicates that the chemical concentrations of reactants and products of ion-exchange reactions do not represent their actual activities. A theory of the activity coefficients of interphase species is necessary just like it is available for free ionic species in bulk solutions where the activities can be obtained from the chemical concentrations with the activity coefficients evaluated by the Debye-Hückel theory.

One common approach applied to ion-exchange resins and organic polyelectrolytes in solution to express their activities is to regard the interphase as a concentrated internal solution phase which is in a Donnan equilibrium (3,

4). With this interphase model, the activity of adsorbed ions is evaluated by using the Donnan potential. However, the observed dependence of the activity coefficients on electrolyte concentrations has shown deviations from those predicted by ideal Donnan theory. This discrepancy has been ascribed to heterogeneity in the resin structure, interactions between co-ions in the resin phase, and variations in the electric potential of the adsorbed co-ion. It has been concluded that "The Donnan theory is valid only for homogeneous exchangers and constant electric potentials within the resin, and under certain practical conditions it is not strictly applicable" (3) and that "No theory has yet succeeded in predicting ion-exchange selectivities, though attempts have been made" with the Gibbs-Donnan theory (4).

For solid compounds like metal oxides and other inorganic exchangers, the surface can be defined more accurately as a two dimensional phase than is possible with resins and organic polyelectrolytes, and approaches to determining activity coefficients, that consider the structures and properties of the interphase, have been employed. The solid surfaces are charged by the protonation and deprotonation of surface functional groups or by the specific adsorption of ions. The charged surface adsorbs counter ions in solution to form an electrical double layer (EDL). Electric neutrality is preserved in the two regions separated by the boundary between the EDL and the bulk solution. In the solution within the EDL, however, the electric neutrality conditions are not upheld and there is an electric potential difference (surface potential) between the solid and the solution. The effect of the surface potential on ion-exchange adsorption has been modeled by Stumm and co-workers, and several electrostatic models have been developed as described in many books and papers (5-22). In these models the mass-action law relations expressed with chemical concentration terms are modified by introducing surface-potential terms. The surface-potential terms are different for different models depending on the assumptions made on the distribution of counter ions in the EDL, as have been named the constant capacitance, the diffuse double layer, and the triple or multilayer models. These electrostatic models have been intensely studied because different properties of various ions and solid exchangers can be formulated universally in terms of the electric charges or potentials. Also,

such models are used widely because of their easy application to adsorption data due to a variety of computer codes available.

These electrostatic models however show a number of shortcomings when applied to "real" oxide samples found in environments and industry:

1. Electrostatic models for solid exchangers have borrowed the EDL theory for metal electrodes and assumed a similar physical significance to the EDL parameters. To conform to the assumed EDL structure of the interface, the electrostatic models require a well-defined solid-solution interface, i.e., a smooth surface with uniform chemical composition and regular crystal structure. However, such an ideal interface is seldom realized in solid exchangers as internal surfaces such as micropores, crevices, and flaws have been shown to exist in metal oxide samples (23-25). Even with ideal surfaces the electric charges on solids due to discrete, charged functional groups and specifically adsorbed ions would be different from those on conductive metal electrodes which are homogeneous due to the very small, quickly moving electrons. As a result, it has been found that the EDL parameters of solid exchangers like the capacitance obtained by applying the electrostatic models show unusual features: the capacitance values are smaller than those typical for metal-electrode electrolyte-solution interphases and the capacitance values differ in the high and low pH regions with respect to the pzc of exchangers (17).

2. Nonelectrical lateral interactions between interface species, such as geometric, chemical, and other interactions, are not considered in the electrostatic models. However, steric (geometric) hindrance is very likely to affect the adsorption of cations on metal oxide because small surface protons are replaced by larger cations (26). Further, for fatty acids adsorbed on mercury the promotive lateral interaction have been suggested to be due to 2-D association, to explain deviations from the Langmuir isotherm (27).

3. The validity of the electrostatic models cannot be substantiated experimentally because the surface potential cannot be measured directly or controlled externally. Also, all the electrostatic models are equally good in fitting experimental data and are indistinguishable, although the model parameter values differ depending on the model chosen (5).

Thus no particular electrostatic model can be used without some ambiguity remaining, and the EDL parameter values determined do not necessarily have the significance assigned to them. Due to these drawbacks of the electrostatic models, there have been warnings against the use of the electrostatic models, as indicated by the following statements by Westall and Drever: "It is important to bear in mind the operational nature of the electrostatic models and not to attach too much physical significance to the value of parameters" (9); "Drawing conclusions about the physical nature of the surface through the use of multilayer double layer models is inappropriate" (11); and "The electrostatic models should not be regarded as a literal description of processes occurring at the molecular scale" (20).

Experimental validation of the mechanistic approaches employed by the previous electrostatic models may be beyond the scope of present-day sciences as it would need to substantiate the molecular features of the solid-solution interfaces.

In a previous review paper (28), it was concluded that the Frumkin equation, a general, thermodynamic model, is more appropriate than electrostatic models when evaluating ion-exchange reactions on metal oxides. The Frumkin model contains two constants for one site, an equilibrium constant of the ion exchange and a constant for the lateral interactions between interphase species. The measured equilibrium amounts of adsorbed ions on metal oxides can be formulated and reproduced with the Frumkin model, and with the constants as universal measures the properties of ions and metal oxides have been evaluated. In that evaluation, the different affinities of ions for oxides were discussed in terms of the charge, size, and hydration state of the ions. The different functions of metal oxides in adsorption were interpreted in terms of the electronegativity of lattice metal ions and the size and morphology of internal pore surfaces on which the adsorption sites are distributed.

In the present article, the results of the application of the Frumkin model to reactions on ion-exchange resins are also included. The model has been found to apply and the different functions of Amberlite IRC-84, a gel-type, and IRC-50, a macroreticular (MR)-type weak acid resins, are discussed in terms of different pore environments around the carboxyl sites.

The lateral interaction term of the Frumkin model expresses the ratio between the activity coefficients of individual interphase species. The changes in the lateral interaction term with ion loading indicate that the respective activity coefficients constituting the lateral interaction term are functions of the surface coverage. A theory of the activity coefficients of interphase species has not been established as described above, and a formulation of the activity coefficient is attempted by considering the interaction between interphase species in a 2-D phase.

## 2. THE FRUMKIN MODEL

With the Frumkin equation, the concentration ratio (apparent constant)  $K$  defined by the mass-action law is formulated as

$$K = K^\circ \exp\{-r\theta/(RT)\} \quad [1]$$

where  $K^\circ$  is the "intrinsic" equilibrium constant,  $\theta$  is the surface coverage, and  $r$  is the lateral interaction constant (29-32). If the sign of  $r$  is positive, Eq. [1] describes that the mass-action relation  $K$  decreases exponentially with increasing surface coverage  $\theta$ , that is, there is suppression of adsorption with increasing ion loading. On the contrary, with decreasing surface coverage, the exponential term approaches to 1, and the mass-action relation  $K$  becomes equal to  $K^\circ$ , a constant. Therefore, at low coverages, the Frumkin equation coincides with the Langmuir equation which is based on the mass-action law.

The underlying assumption of Eq. [1] is that the Gibbs free energy change  $\Delta G$  increases linearly with coverage owing to suppressive lateral interactions between interphase species like electrostatic repulsion, steric hindrance, and others, as

$$\Delta G = \Delta G^\circ + RT \ln Q + r\theta \quad [2]$$

where  $\Delta G^\circ$  is the standard Gibbs free energy change and  $Q$  is the concentration ratio. At equilibrium,  $\Delta G = 0$  and  $Q = K$ , and Eq. [2] becomes Eq. [1] by setting

$\exp\{-\Delta G^\circ/(RT)\}$  as  $K^\circ$ , and the quantity  $r$  represents the extent of suppression.

The sign of  $r$  is positive for suppression, but it is negative for promotive lateral interactions like the association of fatty acids adsorbed on mercury (27).

The assumption of linear variations in the Gibbs free energy change in Eq. [2] covers all factors which cause lateral interactions without making assumptions about the microscopic details of the interphase, and the Frumkin model derived with this assumption is macroscopic and general.

The constant capacitance model as one of the electrostatic models has the same form as the Frumkin equation [1], and the EDL capacitance corresponds to the lateral interaction constant  $r$  in Eq. [1] (33). With the constant capacitance model, the capacitance is limited to values appropriate for parallel plate capacitors. If the capacitance values obtained by fitting the constant capacitance model to ion exchange data fall outside a reasonable range of capacitance of the metal-solution interphase, then the modeling premises are not upheld and the EDL assumptions are not sustainable. Such unexpected capacitance values are very probable (17) because the EDL of organic and inorganic solid exchangers can be greatly different from that of metal electrodes, and in such cases the constant capacitance model would fail to characterize the ion exchange adsorption behaviors.

However, when the Frumkin model is applied to the same data, the model does not limit the lateral interaction to the electrostatic interaction alone, the proportionality constant  $r$  is not restricted to the microscopic assumptions for EDL, and can take any value that can be seen to represent general interaction energies. Thus far, the actual  $r$  values determined have suggested the effect of a variety of factors in the lateral interactions. The factors include the size and hydration state of ions, association of hydrophobic molecules, internal surfaces of oxides such as pores, crevices, and flaws, polarization of surface complexes, nano- and macropore environments around carboxyl sites, and others (27, 28, 34-51).

There have also been other non-mechanistic models like the Freundlich, Tóth, Dobinin-Radushkevic, Redlic-Petersen, Högfeld, and other isotherms (52-55). These models describe ion-exchange data and the model parameters

obtained have been a measure of the abilities and affinities of ions and exchangers. However, they are not derived from molecular nor thermodynamic principles, may be called "empirical", and the concentration and adsorption-density ranges where they apply are limited. To "explain" (not only to describe) ion-exchange phenomena scientifically, a model developed from the behaviors of reactants and products on a very simple, basic level is necessary.

The Frumkin model expressed by Eq. [1] may be taken to be more theoretical since it is based on thermodynamic principles, and it obeys, in principle, the mass-action law as described above.

### 3. ION-EXCHANGE REACTIONS ON METAL OXIDES

Metal oxides are major mineral components of soils and sediments, and also raw materials for ceramics. It is proposed that the hydrous oxides of manganese and iron, in general, furnish the principal control on the fixation of cobalt, nickel, copper, and zinc ions in soils and fresh water sediments (56). In ceramics processing with metal oxides, particle surface-charges affecting the coagulation and dispersion of the particles and so the quality of the final products result from ion-exchange reactions on oxides (57). The sites for ion exchange on metal oxides are surface hydroxyl groups formed by hydration. This section describes first the amount and the formation mechanism of surface hydroxyl groups as ion-exchange sites, and then discusses the ion-exchange properties of oxides and ions evaluated with the parameters obtained by applying the Frumkin model [1].

#### 3.1 Surface hydroxyl sites

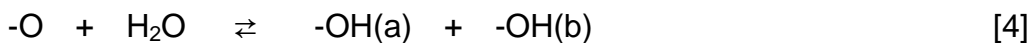
The functional groups relevant to ion-exchange reactions on metal oxides are surface hydroxyl groups, -OH. Most of the surface hydroxyl site densities  $N_s$  ( $\text{mol m}^{-2}$ ) in Table 1 have been obtained with a system shown in Fig. 1 by measuring the amount of methane evolved due to the following reaction with methyl magnesium iodide, a Grignard reagent, with samples where physically adsorbed water had been removed (58).



The other data obtained with NaOH were based on the reaction between acid hydroxyl sites and NaOH, a base. The amount of acid hydroxyl sites was

determined from the amount of NaOH consumed by the acid-base reaction, and was doubled to evaluate the total surface hydroxyl site density  $N_s$ . The  $N_s$  values in Table 1 are similar for different oxides with di-, tri-, and tetra-valent metals.

A new mechanism of hydroxylation has been proposed (59). Oxide ions are larger than metal ions, packed closely in oxides, and the metal oxide lattice terminates with the large oxide ions, -O (60). Figure 2 shows that the terminal oxide ions exposed to the outside as Lewis bases are subject to dissociative chemisorption of water as



The -OH(a) is originally a surface oxide ion to which the proton of a hydrated water molecule is transferred and acts as an acid owing to the positive electric field due to the surrounding lattice metal ions. The -OH(b) is originally a water molecule and without metal ions in direct contact, it acts as a base owing to a less positive electric field. The numbers of acid and base hydroxyl sites are equal as these are formed by the dissociation of neutral water molecules.

According to this hydroxylation mechanism, the surface hydroxylation is initiated by the hydration of surface oxide ions. Then the surface hydroxyl site density would be similar for different oxides because oxide ions in oxides may be regarded to be closely packed and the number of oxide ions in oxides is constant irrespective of the kind of metal ion, in accordance with the observed results.

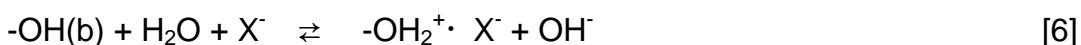
In the conventional mechanism, however, the hydroxyl groups on oxides have been considered to be formed by the hydration of surface metal ions as Lewis acids (6). The hydrated water molecule dissociates to become a hydroxyl group, and the released proton reacts with a neighboring surface oxide ion to form the other hydroxyl group. With this mechanism the surface hydroxyl site density would be different for different oxides, since the number of metal ions in oxides changes with valency. This does not agree with the results shown here.

### 3.2 Monovalent ion adsorption

**Measurements of the amounts of monovalent ions adsorbed** To determine the amount of monovalent ions adsorbed by metal oxides, weighed

portions of metal oxide powder samples ( $\text{MnO}_2$ ,  $\text{Al}_2\text{O}_3$ ,  $\text{TiO}_2$ ,  $\text{Fe}_3\text{O}_4$ ,  $\text{Fe}_2\text{O}_3$ ) were dispersed in 200-cm<sup>3</sup> solutions of 0.1 mol dm<sup>-3</sup> alkali metal nitrate, MX. Nitrogen was bubbled through, and suspensions were allowed to stand for 2-3 h to remove carbon dioxide. Fixed amounts of alkali metal hydroxides (MOH) were added, and the suspensions were titrated with nitric acid solutions with known concentrations at 25°C (Figure 3, curve A). The points in the titration curve were determined after the pH became stable, and the pH was plotted against the amount of nitric acid added,  $n(\text{HNO}_3)$ . In the slowest case, more than 3 h were allowed to assure the attainment of equilibrium. As a reference, titrations were also carried out for MOH-MNO<sub>3</sub> solutions without the oxides (Figure 3, curve B). The two curves deviate, showing the effect of acid-base reactions of the metal oxide. Here, the oxide samples do not dissolve in solution and the acid-base reactions are surface phenomena due to the dissociation of acid and base surface hydroxyl groups.

**Stoichiometry** The acid and base surface hydroxyl groups dissociate according to solution pH, the resulting charged sites attract ions from the external solution to maintain electric neutrality, and the overall result is an ion exchange reaction. For solutions containing simple 1:1 electrolytes, MX, (the oxide-monovalent ion system here), the reactions can be described by



In Eq. [5], acid hydroxyl groups -OH(a) release protons and create negative sites where cations, M<sup>+</sup>, are adsorbed. In Eq. [6], base hydroxyl groups -OH(b) release hydroxide ions and create positive sites where nitrate ions, X<sup>-</sup>, are adsorbed. The dots between the charged sites and adsorbed ions in Eqs. [5] and [6] indicate that the adsorbed ions are located in the solution phase and form an electrical double layer with the charged sites as shown in Fig. 4. This type of adsorption is called "nonspecific", the bond is ionic in nature possibly with water molecules in between, and the products may be called "loose ion-site pairs".

The reaction stoichiometry and the state of adsorbed ions in Eqs. [5] and [6]

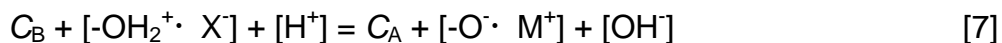
were deduced from the following experimental results:

- 1) measurements of the acidity and basicity of the solution and amounts of ions adsorbed by the oxide showed that the amount of adsorbed monovalent cations or anions is equivalent to that of released protons or hydroxide ions (61-63);
- 2) electrophoretic mobility measurements showed that oxide particles with cations adsorbed migrate to a positive electrode and those with anions to a negative electrode, indicating that the oxide surface has charges with a sign opposite to that of the adsorbed ions (64).

Here, the surface acid and base reactions that cause surface charges are cation and anion exchange reactions [5] and [6]. A simple ion salt MX is therefore not an indifferent electrolyte for surface charge formation, the respective cations and anions are reactants, and they appear in the mass-action relations in the "equilibrium condition" section below.

Application of the electric balance principle to the two titration curves in Fig. 3 leads to the following two equations:

For curve A,



For curve B,



where  $C_A$  is the added concentration ( $\text{mol dm}^{-3}$ ) of strong acid, HA, for the suspension or the concentration of the anion,  $A^-$ , from the acid;  $C_A'$  is the added strong acid concentration for the blank solution;  $C_B$  is the added concentration of strong base, BOH, or the concentration of the cation,  $B^+$ , from the base; and the square bracket terms for  $-OH_2^+ \cdot X^-$  and  $-O^- \cdot M^+$  are the amounts of positive and negative sites per unit volume of the solution ( $\text{mol dm}^{-3}$ ). Here, the concentrations of  $M^+$  and  $X^-$  from the salt MX do not appear in the equations because the sum of the concentrations of adsorbed and unadsorbed  $M^+$  is equal to that for  $X^-$  and they cancel out.

The concentration  $C_B$  of the base is set as common to curves A and B, and subtraction of Eq. [8] from Eq. [7] at the same pH gives the following equation:

$$[-\text{OH}_2^+ \cdot X^-] - [-\text{O}^- \cdot M^+] = C_A - C_A' \quad [9]$$

Equation [9] indicates that the difference in the concentrations of acid added to the suspension and the blank solution is equal to the difference in the concentrations of positive and negative sites. Multiplying both sides of Eq. [9] by the solution volume  $V$  ( $\text{dm}^3$ ) leads to

$$n(-\text{OH}_2^+ \cdot X^-) - n(-\text{O}^- \cdot M^+) = \Delta x \quad [10]$$

where  $n$  is the amount of the respective species (mol) and  $\Delta x$  is the difference in the amounts of acid added. The value of  $\Delta x$  can be obtained from the deviation of the titration curves in Fig. 3. Dividing both sides of Eq. [10] by the surface area of the oxide particles in the solution,  $S$  ( $\text{m}^2$ ), leads to

$$\langle -\text{OH}_2^+ \cdot X^- \rangle - \langle -\text{O}^- \cdot M^+ \rangle = \Delta x/S = \sigma \quad [11]$$

where the  $\langle \rangle$  bracket stands for the amount of charged sites per unit surface area (surface density,  $\text{mol m}^{-2}$ ) and the difference in the surface densities of positive and negative sites is the surface-charge density expressed by  $\sigma$  ( $\text{mol m}^{-2}$ ). Further conversion of the charge expressed with the amount of substance (mol) to the electricity (C) by multiplying the Faraday constant is not made and so the charge can be directly related to the amount of ions adsorbed. The  $\sigma$  value is obtained from the  $\Delta x$  in Fig. 3, and where the A and B curves intersect,  $\sigma$  is zero and this pH is the point of zero charge (pzc).

It is also possible to obtain  $\sigma$  from Eq. [7] alone with the values of the ionic product of water  $K_w$ ,  $C_A$ ,  $C_A'$ ,  $C_B$ , and pH (65). With this method the values of  $\sigma$  would contain uncertainties due to possible errors in these five quantities. However, with the blank subtraction method used here, the comparison of the two titration curves is made at the same pH, and  $\sigma$  is determined from only two quantities  $C_A$  and  $C_A'$ ; as a result the  $\sigma$  values measured here have higher accuracies.

The values of  $\sigma$  for various oxides obtained from  $\Delta x$  at ionic strength 0.1  $\text{mol dm}^{-3}$  ( $\text{NaNO}_3$ ) and 25°C are shown in Fig. 5. Positive sites are predominant

at low pH, and negative sites at high pH. The charge behavior is similar for different oxides, but the pzc values are different. Figure 6 shows the  $\sigma$ -pH relation for  $\text{MnO}_2$  (IC12) with different alkali metal nitrates. The  $\sigma$ -pH curves converge with decreasing pH and the pzc appears to be common to these alkali metal ions. At high pH, the amount of negative sites is apparently larger for the alkali metal ions with lower atomic number.

The change in  $\sigma$  with changing proton concentration is very small, since  $\sigma$  is plotted on a normal scale while the proton concentration is on a log scale as pH. Apparently, the formation of charged sites is subject to suppression with increasing pH, i.e., the progress of ion exchange. The charge characteristics of the oxide surfaces are modeled in the following (28, 37, 40, 42, 47).

**Material balance** According to the reaction equations [5] and [6], the material balance equations for acid and base surface sites are given by

$$\langle -\text{OH}(a) \rangle + \langle -\text{O}^- \cdot \text{M}^+ \rangle = N_s/2 \quad [12]$$

$$\langle -\text{OH}(b) \rangle + \langle -\text{OH}_2^+ \cdot \text{X}^- \rangle = N_s/2 \quad [13]$$

where  $N_s/2$  is the anion or cation exchange capacity, equal to the sum of the surface densities of dissociated and undissociated hydroxyl sites. It is assumed here that the hydroxyl sites measured by the Grignard method are all taking part in ion exchange.

**Equilibrium conditions** For the mass-action relations between the species taking part in reactions [5] and [6], the concentration ratios  $K_a$  and  $K_b$  are defined as

$$K_a = \langle -\text{O}^- \cdot \text{M}^+ \rangle [\text{H}^+] / (\langle -\text{OH}(a) \rangle [\text{M}^+]) \quad [14]$$

$$K_b = \langle -\text{OH}_2^+ \cdot \text{X}^- \rangle [\text{OH}^-] / (\langle -\text{OH}(b) \rangle [\text{X}^-]) \quad [15]$$

The extent of the progress of the reactions is given by the following surface coverages  $\theta_a$  and  $\theta_b$ , that is the fractions of the acid and base hydroxyl sites occupied by adsorbed ions:

$$\theta_a = \langle -\text{O}^- \cdot \text{M}^+ \rangle / (N_s/2) \quad [16]$$

$$\theta_b = \langle -\text{OH}_2^+ \cdot X^- \rangle / (N_s/2) \quad [17]$$

The apparent suppression of the formation of charged sites with the progress of ion exchange reactions [5] and [6] may be owing to electrostatic, geometric, and other lateral interactions between interphase species as suggested above. The equilibrium condition equations for these exchange reactions can be defined by applying the Frumkin model [1], like

$$K_a^\circ = K_a \exp (A_a \theta_a) \quad [18]$$

$$K_b^\circ = K_b \exp (A_b \theta_b) \quad [19]$$

where  $K_a^\circ$  and  $K_b^\circ$  are the "intrinsic" equilibrium constants;  $K_a$  and  $K_b$  are the concentration ratios at equilibrium; and  $A_a$  and  $A_b$  are the lateral interaction constants, being  $A_a=r_a/(RT)$  and  $A_b=r_b/(RT)$ . The equilibrium constants of ion exchange reactions here are the acid and base dissociation constants of surface hydroxyl groups and the stability constants of ion-site pairs as well. The exponential terms express the suppression of ion exchange by already formed ion-site pairs. The values of  $A_a$  and  $A_b$  are measures of the suppression effect owing to the lateral interactions between interphase species.

**Fitting the model equations to data** The logarithmic form of Eqs. [18] and [19] in general is:

$$\log K = \log K^\circ - \theta A \log e \quad [20]$$

where  $e$  is the base of the natural log.

In the pH regions one pH unit above or below pzc, it is likely that one exchange reaction is predominant and the other exchange reaction can be disregarded owing to the opposite pH dependencies of the reactions. Then, the absolute values of  $\sigma$ ,  $|\sigma|$ , can be regarded as equal to  $\langle -\text{O}^- \cdot M^+ \rangle$  or  $\langle -\text{OH}_2^+ \cdot X^- \rangle$ , and the  $K$  and  $\theta$  values can be calculated with the measured  $\sigma$  as  $K_a=|\sigma|[\text{H}^+] / ([N_s/2-|\sigma|][M^+])$ ,  $K_b=|\sigma|[\text{OH}^-] / ([N_s/2-|\sigma|][X^+])$ ,  $\theta_a=|\sigma|/(N_s/2)$ , and  $\theta_b=|\sigma|/(N_s/2)$ . With these it is possible to analyze the measured data by a graphical method, and the  $\log K_a$  values for an  $\text{MnO}_2$  sample (IC12) were plotted against  $\theta_a$

according to Eq. [20] (Fig. 7). It is seen that  $\log K_a$  decreases linearly with increasing  $\theta_a$ , demonstrating the good fit to Eq. [20]. The intercepts of the straight lines provide  $K_a^\circ$  values and the slopes provide  $A_a$  values. The good linearity indicates only one kind of reaction with respect to both the reactivity and the lateral interaction. The applicability of the graphical method to surface acid-base dissociation data has been shown by Stumm for FeOOH (65).

Nonlinear regression analysis can also be used to examine the suitability of the model equations to the data and to determine the model parameters (66-68). With this method all the data for cation and anion exchange reactions can be fitted to Eqs. [11] - [19] simultaneously, and the four unknown constants were determined as the optimum values of the model parameters according to the procedure described elsewhere (28, 37, 48). The results obtained by the graphical and nonlinear regression methods are shown in Tables 2 and 3. The best fit parameter values reproduce the measured  $\sigma$  (Figs. 5 and 6) and the concentration ratio  $K_a$  (Fig. 7) changing over more than four orders of magnitude (40, 42, 47).

**Adsorption abilities of metal oxides for monovalent ions** The ion adsorption reactivities of metal oxides for monovalent ions can be evaluated

with the values of the equilibrium constants,  $K_a^\circ$  and  $K_b^\circ$ . It is expected that the

$K_a^\circ$  and  $K_b^\circ$  values may be explained by the electronegativity of the oxides, since the bonding of exchanging protons or hydroxide ions to metal oxides is determined by the density of electrons on lattice oxide ions.

Tanaka and Ozaki (69) reported the following equation for the electronegativity,  $X_i$ , of the lattice metal ions of oxides:

$$X_i = (1 + 2Z)X_0 \quad [21]$$

where  $Z$  is the charge of the metal ions and  $X_0$  the electronegativity of the corresponding elemental metals. This equation was developed from the relation  $X_i = (\partial I / \partial Z)$ , where  $I$  is the ionization potential of the metals, a polynomial of  $Z$ .

The  $X_i$  values were calculated for the metal oxides examined in this

investigation, and  $\log K_a^\circ$  and  $\log K_b^\circ$  for  $\text{NaNO}_3$  were plotted against  $X_i$  (Fig. 8). The charge of iron ions in  $\text{Fe}_3\text{O}_4$  was assumed to be an average +2.7. It is seen that  $\log K_a^\circ$  increases while  $\log K_b^\circ$  decreases with  $X_i$  in a symmetrical way, though  $\text{Fe}_3\text{O}_4$  shows some deviation. With increasing electronegativity of lattice metal ions, the electron density of adjacent lattice oxide ions would decrease. Then the acid hydroxyl site would lose its proton more easily, leading to a larger  $K_a^\circ$ ; opposite, the base hydroxyl site would gain a proton (lose a hydroxide ion) with difficulty, leading to a smaller  $K_b^\circ$ .

The deviation of  $\text{Fe}_3\text{O}_4$  from the correlation curves was attributed to the oxidation of iron ions on magnetite surfaces with a  $Z$  value larger than 2.7 (48). With the real  $X_i$  value larger than 2.7, the points for magnetite in Fig. 8 would shift rightwards, approaching to the correlation curves.

The  $\text{MnO}_2$  samples prepared under different conditions for battery purposes (IC1, 12, and 22) showed differences in the values of  $K_a^\circ$  and  $K_b^\circ$ , suggesting that factors other than the electronegativity affect the acid-base properties of oxide surfaces; such factors would include the crystal structure, the bond length in the oxide lattice, the morphologies of surfaces, the pore structure, and others. However, the differences in  $K_a^\circ$  and  $K_b^\circ$  among the  $\text{MnO}_2$  samples are at most about one order of magnitude, and there are much larger differences with different oxides. It may be concluded that electronegativity, different with the kind of oxide, plays a major role in determining the acid-base properties of surface hydroxyl groups.

The differences in the suppression constants,  $A_a$  and  $A_b$ , for different oxides with  $\text{NaNO}_3$  in Table 2 suggest that the oxides have different properties as media for adsorbed ions to interact mutually. These differences would be owing to different geometrical conditions at the oxide/solution interphases with which geometric arrangements of adsorbed ions are determined; and it has been

suggested that the metal oxide samples have different surface morphologies and micro-structures due to pores, crevices, flaws, etc. (58, 59). The pore diameter of electrolytic manganese dioxide has been evaluated to be around 4 nm (23), this size is large enough to accommodate hydrated alkali metal ions with diameters around 0.5 nm. On such internal surfaces, there would be interactions due to ions adsorbed on opposite walls (across-pore interaction) in addition to interactions between adjacent ions, all playing a role in suppressing adsorption (Fig. 9). Further, different electric charge densities on the charged sites would be another cause for differences in lateral interactions. The density of positive charge on  $\text{-OH}_2^+$  sites would increase with increasing electronegativity, since electrons on oxide ions are attracted more strongly to lattice metals. With a large charge density at the positive site, the negative charge on the adsorbed nitrate ions would be neutralized and the polarization of the ion-site pair would decrease. Then, the electric repulsion between the ion-site pairs would become smaller, and in Table 2 the lateral repulsion ( $A_b$ ) apparently decreased with increasing electronegativity (from bottom to top). The electric charge density on  $\text{-O}^-$  sites would also decrease with increasing electronegativity, however, the  $A_a$  values do not show any apparent correlation with the electronegativity. The adsorbed alkali metal ions are strongly hydrated as will be described next, and the hydrated water molecules would be a barrier to the electron transfer between surface sites and adsorbed sodium ions. The electric charges on adsorbed hydrated sodium ions do not seem to be neutralized effectively by the  $\text{-O}^-$  sites.

**Adsorption affinities of alkali metal ions** The adsorption reactivity of alkali metal ions for  $\text{MnO}_2$  (IC12) evaluated from  $K_a^\circ$  increases with the atomic number of the alkali metal ions. The lateral repulsion evaluated from  $A_a$  also increases with the atomic number (Table 3). Alkali metal ions are hydrated with the hydrated-ion diameter decreasing in the atomic number order (70), and hence the charge density of hydrated alkali metal ions increases with the atomic number. The increase in both  $K_a^\circ$  and  $A_a$  with atomic number indicate that the alkali metal ions adsorbed are in a state of hydration as the "nonspecific"

adsorption was assumed in the model here. A similar increasing reactivity series with decreasing hydrated-ion diameters has been shown by Amphlett (71). However, Fig. 6 indicates that at high pH the amount of adsorbed ions decreases with the atomic number, this order is apparently opposite to the reactivity ( $K_a^\circ$ ) order. This apparent discrepancy between the adsorption reactivity and the observed amount of adsorbed ions is due to strong lateral repulsion at high coverages. At high pH and hence at high coverages, the exponential term containing  $A_a\theta_a$  becomes large, and the  $K$  order becomes opposite to the  $K^\circ$  order as seen from Fig. 7.

**Distribution of surface ion-pairs vs. pH** With the use of the established constants, the extent of the reaction (formation of ion-site pairs) can be calculated as a reverse process to that of determining the constants. As an example, the surface densities of ion-site pairs on  $\text{Fe}_3\text{O}_4$  were obtained as a function of pH at an ion concentration of  $0.1 \text{ mol dm}^{-3}$  ( $\text{NaNO}_3$ ) by solving the model equations and by calculating the surface densities from  $\theta N_s/2$  (Fig. 10). The density of negative site-cation pairs increases and that of positive site-anion pairs decreases with pH, and they intersect at pzc. At pzc,  $\theta_a=\theta_b=\theta_0$  and the surface density of charged sites  $\Gamma_0$  is given by  $\theta_0 N_s/2$ . The undissociated acid and base hydroxyl sites predominate over a wide pH range. As Fig. 10 shows, the model calculations enable a prediction of the extent of ion adsorption and the surface charge for given conditions.

At pzc, the concentrations of cations and anions in solution are also equal, and dividing Eq. [18] by Eq. [19] at pzc leads to

$$\text{pzc} = \{\text{p}K_a^\circ - \text{p}K_b^\circ + \text{p}K_w + 2(A_a - A_b)\theta_0 \log e / N_s\}/2 \quad [22]$$

where  $K_w$  is the ion product of water ( $10^{-14} \text{ mol}^2 \text{ dm}^{-3}$  at  $25^\circ\text{C}$ ). Also, multiplying Eq. [18] by Eq. [19] at pzc leads to

$$K_w \theta_0^2 \exp\{2(A_a + A_b)\theta_0/N_s\} = K_a^\circ K_b^\circ C^2(N_s/2 - \theta_0)^2 \quad [23]$$

where  $C$  is the concentration of MX added, equal to the bulk anion and cation

concentrations under the experimental conditions here. Equation [23] can be solved for  $\theta_0$ , and by using this  $\theta_0$  the pzc can be calculated from Eq. [22]. The calculated pzc values are shown in Table 2, and they agree well with those obtained graphically from Fig. 5.

It has been widely believed that the pzc is a constant for different concentrations of electrolytes constituted of ions to be adsorbed nonspecifically.

However,  $K_a^\circ$ ,  $K_b^\circ$ ,  $K_w$ ,  $A_a$ ,  $A_b$ , and  $\theta_0$  are functions of the electrolyte concentration as described above, and Eq. [22] suggests that the pzc could vary with the ionic strength of a solution.

### 3.3 Divalent Metal Ion adsorption

**Measurements of the amounts of divalent metal ions adsorbed** Metal oxide powder samples ( $\text{MnO}_2$ ,  $\text{Fe}_2\text{O}_3$ ,  $\text{Al}_2\text{O}_3$ ,  $\text{TiO}_2$ ,  $\text{Fe}_3\text{O}_4$ ) were dispersed in solutions containing divalent heavy metal ions  $M^{2+}$  ( $\text{Cu}^{2+}$ ,  $\text{Mn}^{2+}$ ,  $\text{Co}^{2+}$ ,  $\text{Ni}^{2+}$ ,  $\text{Cu}^{2+}$ ,  $\text{Zn}^{2+}$ ) and  $0.1 \text{ mol dm}^{-3}$   $\text{NaNO}_3$  at different pH adjusted with  $\text{HNO}_3$  and  $\text{NaOH}$ . The suspensions were shaken at  $25^\circ\text{C}$  to reach equilibrium ( $\sim 12\text{h}$ ), after the separation of solid and solution, the equilibrium pH was measured, and the equilibrium concentration of  $M^{2+}$  in solution,  $[M^{2+}]$  ( $\text{mol dm}^{-3}$ ), was determined by the radioactive tracer method for  $\text{Co}^{2+}$  and by atomic absorption spectrometry for the other ions. The amount of adsorbed  $M^{2+}$  was obtained from the difference between the total concentration of  $M^{2+}$  added,  $[M^{2+}]_T$ , and the equilibrium concentration,  $[M^{2+}]$ , multiplied by the solution volume  $V$  ( $\text{dm}^3$ ). The amount of adsorbed  $M^{2+}$  per unit surface area, the surface density  $\Gamma$  ( $\text{mol m}^{-2}$ ), was obtained by dividing the amount of adsorbed metal ions by the surface area of the oxide samples,  $S$  ( $\text{m}^2$ ), according to

$$\Gamma = ([M^{2+}]_T - [M^{2+}]) V / S \quad [24]$$

The obtained  $\Gamma$  values were plotted against  $[M^{2+}]$  for set pH values as adsorption isotherms. The pH and ion concentration were set so that metal ions exist as free aqua ions and the hydrolyzed species are minor constituents ( $\text{pH} \leq 7.5$ ,  $[M^{2+}]_T \leq 10^{-3} \text{ mol dm}^{-3}$ ). As an example, Figure 11 shows adsorption isotherms for  $\text{Co}^{2+}$  ions on magnetite,  $\text{Fe}_3\text{O}_4$ , where both  $\Gamma$  and  $[\text{Co}^{2+}]$  are plotted on log scales. The log  $\Gamma$  values increase with pH and also with log  $[\text{Co}^{2+}]$ .

The  $\log \Gamma$ - $\log [Co^{2+}]$  curves have a slope of one at very low  $\Gamma$  values, and the slope decreases with increasing  $\log \Gamma$  or  $\log [Co^{2+}]$ .

The other  $M^{2+}$ -metal oxide systems show adsorption isotherms similar to Fig. 11.

If polynuclear hydroxo complexes, minor constituents in solution at the pH and ion concentration values here, were adsorbed as suggested by EXAFS, ENDOR, and other X-ray absorption studies (72-76) and in equilibrium with  $M^{2+}$ , then the slope would be steeper than one, since the concentration of polymers is proportional to the monomer concentration with the power of the number of monomers in the polymer. Slopes steeper than one were however not observed in any of the isotherms and for all the ions examined in this investigation, it was concluded that the monomeric ions in solution reacted with the surface. In the EXAFS experiments, the solution pH and ion concentrations were higher than here to ensure sufficient amounts of adsorbed species to meet the sensitivity limit of the spectroscopy. These experimental conditions may have facilitated the formation of hydroxo polymers and hydroxides.

**Stoichiometry** The adsorption of divalent metal ions,  $M^{2+}$ , is increased by increasing pH, suggesting that the reaction is an exchange with surface protons. The following exchange reactions are suggested based on the experimental evidence described below:



Reaction [25] is a (1:1)  $M^{2+}/\text{H}^+$  exchange and the resulting oxide surface has a charge of +1, since the adsorbed  $M^{2+}$  donates its positive charge of +2 to the surface with a negative charge of -1 produced by the release of a proton. The net charge of +1 is counter balanced by adsorbing a simple monovalent anion  $X^-$  (here nitrate ions) nonspecifically like in reaction [6]. Reaction [26] is a (1:2)  $M^{2+}/\text{H}^+$  exchange and the net charge is zero. In reactions [25] and [26], the adsorbed  $M^{2+}$  ions belong to the oxide phase, and this type of adsorption is termed "specific". The bond has been regarded to be similar to that of coordination compounds, and the reaction products are called "surface

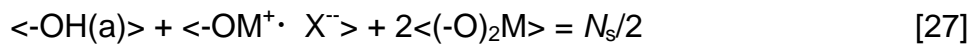
complexes".

The reaction stoichiometry and the state of adsorbed  $M^{2+}$  ions were deduced from the following experimental results:

- 1) measurements of the quantity ratio of released  $H^+$  to adsorbed  $M^{2+}$  gave values between 1 and 2 (2, 39, 77-79), evidencing reactions [25] and [26] to occur simultaneously;
- 2) electrophoretic mobility measurements showed that at a pH where the oxide surface is originally negative, the addition of  $M^{2+}$  changes the surface charge from negative to positive (14, 62, 63, 80-82). This "charge reversal" evidences that the adsorbed  $M^{2+}$  must belong to the solid phase, donating its positive charge to the oxide.

Reactions [25] and [26] indicate that the protons are released from the surface hydroxyl groups. However, previously it has been proposed that protons are released by the dissociation of hydrated water molecules of  $M^{2+}$  with the assumption that the adsorption occurs via hydrolyzed metal ions,  $MOH^+$ , in the pH range where the hydrolyzed metal ions are minor constituents. With this mechanism, the concentration of  $MOH^+$  increases with pH, and the adsorption via this hydrolyzed species increases with pH. This mechanism of adsorption requires that the hydroxo complexes have very high adsorption reactivity to explain the measured extent of adsorption since they are minor constituents. In the previous paper (49), the adsorption reactivity of  $CoOH^+$  was estimated, and the reactivity was more than 10 orders of magnitude higher than that of  $Na^+$ . These are both monovalent ions and such an extremely large difference in the adsorption reactivity is difficult to accept. As commented by Stumm (83), more direct approaches, like kinetic investigations and various spectroscopic observations of interphase species, were in accord with the adsorption of free metal ions and not hydrolyzed species.

**Material balance** For acid hydroxyl sites on which cation exchange reactions take place, the following material balance equation is obtained:



where the  $\langle \rangle$  brackets indicate the surface densities of the respective species ( $\text{mol m}^{-2}$ ),  $N_s$  is the surface density of total hydroxyl sites ( $\text{mol m}^{-2}$ ), and the half

is the cation exchange capacity.

At the acid hydroxyl sites, the other cation  $\text{Na}^+$  is also adsorbed to form  $-\text{O}^- \cdot \text{Na}^+$ . However,  $\text{Na}^+$  ions occupy at most a few percent of the cation exchange capacity of acid hydroxyl sites in the pH range 3.5 - 6.5 as seen in Fig. 10, and the  $[-\text{O}^- \cdot \text{Na}^+]$  term is omitted in Eq. [27].

**Equilibrium conditions** With increasing  $\Gamma$ , the slope starts to decrease from one at  $\Gamma$  values several orders of magnitude lower than saturation for the (1:1) surface complex, which could be estimated to be about  $0.5 \times 10^{-5}$  mol m<sup>-2</sup> from the cation exchange capacity  $N_s/2$ , where the  $N_s$  value is  $1.08 \times 10^{-5}$  mol m<sup>-2</sup> for  $\text{Fe}_3\text{O}_4$  (35). This indicates that the decrease in the slope is not owing to the saturation of the surface but due to a suppression of the ion exchange with the progress of the reaction. Then the equilibrium condition equations for the (1:1) and (1:2) exchange reactions [25] and [26] can be defined by the Frumkin model [1], like

$$K_1^\circ = \frac{\langle -\text{OM}^+ \cdot \text{X}^- \rangle [\text{H}^+]^2}{\langle -\text{OH(a)} \rangle^2 [\text{M}^{2+}]} \exp(B_1 \theta_1) \quad [28]$$

$$\beta_2^\circ = \frac{\langle (-\text{O})_2 \text{M} \rangle [\text{H}^+]^2}{\langle -\text{OH(a)} \rangle^2 [\text{M}^{2+}]} \exp(B_2 \theta_2) \quad [29]$$

where  $K_1^\circ$  and  $\beta_2^\circ$  are the "intrinsic" equilibrium constants;  $B_1$  and  $B_2$  are the lateral interaction constants, being  $B_1 = r_1/(RT)$  and  $B_2 = r_2/(RT)$ ; and  $\theta_1$  and  $\theta_2$  are the coverages of the acid hydroxyl sites with the (1:1) and (1:2) surface complexes, being  $\theta_1 = \langle -\text{OM}^+ \cdot \text{X}^- \rangle / (N_s/2)$  and  $B_2 = 2 \langle (-\text{O})_2 \text{M} \rangle / (N_s/2)$ .

For the (1:1) and (1:2) surface complexes, either of these dominates at a pH because of their different pH dependencies. The minor component affects the formation of the major component only little, the effect of the major component on the minor component may be large, but the contribution of the minor

component to  $\Gamma$  is small. Hence, Eqs. [28] and [29] assume only the interaction between surface complexes of the same kind to analyze and reproduce the observed  $\Gamma$ .

**Fitting the model equations to data** According to the model, the measured surface density of adsorbed ions  $\Gamma$  is the sum of the densities of the two types of surface complexes as

$$\Gamma = \langle -\text{OM}^+ \cdot \text{X}^- \rangle + \langle (-\text{O})_2\text{M} \rangle \quad [30]$$

The surface densities of (1:1) and (1:2) surface complexes corresponding to measured  $\Gamma$  data can be calculated from Eqs. [27] - [29], when the values of the four unknown constants are specified as model parameters. By the nonlinear regression analysis, the calculated  $\Gamma$  with Eq. [30] were compared with the measured  $\Gamma$  for all the data to obtain the sum of the squares of the deviations. Here the parameter values were systematically changed to find the optimum values of the parameters, those that give the least values of the error sum according to the procedure described elsewhere (28, 36, 48).

The values of the constants obtained by fitting the model and optimizing the model parameters are shown in Tables 4 and 5. The curves of the adsorption isotherms in Fig. 11 are the calculations with the best fit parameters, and it is seen that the curves calculated with the four constants reproduce the measured data points ranging over more than three orders of magnitude.

**Adsorption abilities of metal oxides for divalent ions** The values of the constants determined reflect the affinities of ions for the oxides and the abilities of the oxides to adsorb ions. The stability constants,  $K_1^\circ$  and  $\beta_2^\circ$ , for the  $\text{Co}^{2+}$ -oxide surface complexes (Table 4) were plotted against the electronegativity of lattice metal ions of the oxides,  $X_i$ , defined by Eq. [20] (Fig. 12). Except with  $\text{Fe}_3\text{O}_4$ , both  $K_1^\circ$  and  $\beta_2^\circ$  increase and correlate well with  $X_i$ . All

the  $K_1^\circ$  and  $\beta_2^\circ$  terms include  $K_a^\circ$ , since reactions [25] and [26] include the deprotonation process [5]. The reactivities of deprotonated negative sites,

$\text{-O}^-$ , for  $\text{Co}^{2+}$  adsorption were obtained by dividing the stability constants  $K_1^\circ$  and  $\beta_2^\circ$  by  $K_a^\circ$  as  $K_1^{\circ*}=K_1^\circ/K_a^\circ$  and  $\beta_2^{\circ*}=\beta_2^\circ/(K_a^\circ)^2$ . The  $K_1^{\circ*}$  and  $\beta_2^{\circ*}$  change only slightly with  $X_i$  for  $\text{Fe}_3\text{O}_4$ ,  $\text{Fe}_2\text{O}_3$ ,  $\text{TiO}_2$ , and  $\text{MnO}_2$ , and the reactivity of  $\text{-O}^-$  sites for  $\text{Co}^{2+}$  adsorption is insensitive to the decrease in the donor electron density with  $X_i$  (Fig. 13). This suggests that the good correlation of  $K_1^\circ$  and  $\beta_2^\circ$  with  $X_i$  is due to  $K_a^\circ$  and that the deviation of  $\text{Fe}_3\text{O}_4$  here may be due to the deviation in  $K_a^\circ$  described in the "Adsorption abilities of metal oxides for monovalent ions" section. Also, the results here suggest that the bond between the  $\text{Co}^{2+}$  and  $\text{-O}^-$  sites is not a coordination type bond because this type of bond is strongly affected by the electron-pair donation ability of ligands. The  $\text{Co}^{2+}$  surface complexes are likely formed by electrostatic contact adsorption (ionic bond formation) owing to the large positive charge on  $\text{Co}^{2+}$  and the negative charge of -1 on  $\text{-O}^-$  sites. The  $\text{-O}^-$  sites on  $\text{Al}_2\text{O}_3$  showed very high adsorption reactivities,  $K_1^{\circ*}$  and  $\beta_2^{\circ*}$ , suggesting that coordination bond formation occurs here owing to high electron densities caused by the very low electronegativity of  $\text{Al}^{3+}$ . The overall  $\text{Co}^{2+}$  ion adsorption reactivities of  $\text{Al}_2\text{O}_3$ ,  $K_1^\circ$  and  $\beta_2^\circ$ , are however the lowest among these oxides, because this  $\text{-O}^-$  site is bound very strongly with protons.

The correlation with the electronegativity may provide guidelines to describe and predict the different ion adsorption reactivities of metal oxides and metal oxide deionizers. The large  $K_1^\circ$  and  $\beta_2^\circ$  of  $\text{MnO}_2$  for  $\text{Co}^{2+}$  strongly suggest that adsorption plays an important role in the concentration of cobalt in manganese nodules. The large  $K_1^\circ$  and  $\beta_2^\circ$  of  $\text{Fe}_3\text{O}_4$  among oxides in a corrosion scale appear to explain radioactive contamination of cooling systems in nuclear power

plants as due to the incorporation of radioactive  $^{60}\text{Co}^{2+}$  into this oxide through adsorption.

The lateral interaction properties of oxides with divalent metal ions can be discussed with the values of the suppression constants,  $B_1$  and  $B_2$ . The  $B_1$  and  $B_2$  values are different for different oxides (Table 4), suggesting that the adsorbed ions or the adsorption sites are located with geometrically different arrangements. The BET specific surface areas of metal oxides other than  $\text{Fe}_3\text{O}_4$  are much larger than those estimated from the modal diameters of the oxide particles observed by electron microscopy and the densities of the oxides (Table 1). The  $\text{Fe}_3\text{O}_4$  sample here was shown to be non-porous (35), but the other metal oxides would have internal surfaces due to pores, crevices, flaws, etc. (58, 59). Different across-pore interactions between ions adsorbed on internal surfaces (Fig. 9) may be the cause of the different lateral interaction constants of different oxides and this would also explain that metal oxides with larger BET specific surface areas have larger  $B_1$  and  $B_2$  values than  $\text{Fe}_3\text{O}_4$  (Table 4).

**Adsorption affinities of divalent heavy metal ions** The different adsorption reactivities of divalent metal ions can be expressed by the equilibrium constant of the (1:1) surface complex formation  $K_1^\circ$  (Table 5). These ions tend to hydrolyze and the (1:1) hydroxo complex formation is described by



The stability constants of the (1:1) hydroxo complexes,  $K_1^{\text{OH}}$ , were taken from the literature (84) and the relationship between  $K_1^\circ$  and  $K_1^{\text{OH}}$  was examined (Fig. 14). For both  $\text{MnO}_2$  and  $\text{Fe}_2\text{O}_3$ , the ions show good linear relations with a slope of one, except for  $\text{Mn}^{2+}$  ions on  $\text{MnO}_2$ , the deviation of  $\text{Mn}^{2+}$  was explained in terms of the oxidation of this ion by  $\text{MnO}_2$  (49). Similar correlation between adsorption and hydrolysis has also been observed for  $\text{SiO}_2$  and  $\text{FeOOH}$  (85, 86). This correlation may be used to estimate adsorption reactivities of other ions for oxides. The parallel correlation curves indicate that

the ion adsorption reactivity ( $K_1^\circ$ ) ratio between these oxides is constant regardless of the kind of ion adsorbed, as  $K_1^\circ$  is plotted in log scale. Such parallel relations may also hold with other oxides and may be used to evaluate ion adsorption reactivities of other metal oxides.

The good correlation means that ions with higher reactivities to form hydroxo complexes have higher adsorption reactivities. Previously, it was proposed that the adsorption occurs via hydrolyzed species in pH regions where the hydrolyzed species are minor constituents. However, it has been concluded that the adsorbing species are free metal ions, not hydrolyzed species as described above.

Then the good correlation is ascribed to similarities in the chemical bonds in both surface complexes and hydroxo complexes. As a reaction similar to the hydroxo complex formation, the hydration of divalent metal ions in the first transition series may be considered. The hydration energy increases in the order:  $Mn^{2+} < Fe^{2+} < Co^{2+} \sim Zn^{2+} < Ni^{2+} < Cu^{2+}$  (87), this order is very similar to that for the hydroxo complex formation of the ions:  $Mn^{2+} < Ni^{2+} < Co^{2+} < Zn^{2+} < Cu^{2+}$  (Fig. 14, horizontal scale) except for  $Ni^{2+}$ . All these ions have an electric charge of 2+, but the charge density on these ions is different depending on the ionic radii as commonly expressed by the charge/radius ratio. Electrostatic theory, including crystal field corrections, was applied to the different hydration energy of the ions, and then the corrected increasing order of hydration energies coincided with the increasing order of electric charge density of ions, demonstrating the bond to be ionic (87). This means that the bond between the metal ions and water, and hence hydroxide ion is ionic in nature. The adsorption reactivity order (Fig. 14, vertical scale) is therefore very likely to indicate that these reactions are both ionic due to electrostatic attractions between the positive charge of metal ions and the negative charge of deprotonated hydroxyl sites on oxides or hydroxide ions in solution.

From the relationship between the  $Co^{2+}$  adsorption properties of metal oxides and the electronegativity of the oxides, it has been suggested that the  $Co^{2+}$ -metal oxide surface complexes are formed by electrostatic contact

adsorption between  $\text{Co}^{2+}$  ions with positive charges and deprotonated hydroxyl sites  $-\text{O}^-$  with negative charges (48). The findings here for the reactivities of first transition metals in general extend the electrostatic contact adsorption mechanism to other divalent ions.

The correlation between the (1:2) surface complexation and the (1:2) hydroxo complexation, like for the (1:1) complexation above, was not examined because of insufficient (1:2) hydrolysis data.

Different lateral Interaction properties of M(II) Ions can be evaluated with  $B_1$  and  $B_2$ . For the  $\text{Ni}^{2+}$ ,  $\text{Zn}^{2+}$ , and  $\text{Co}^{2+}$  adsorption on all the oxides,  $B_2 > B_1$  (Tables 4 and 5), indicating that the (1:2) surface complex formation is subject to stronger suppression than the (1:1) complex. Figure 15 illustrates the structure and polarization of (1:1) and (1:2) surface complexes. If the M(II) surface complexes are completely polarized, i.e.,  $\delta+=+2$  and  $\delta=-1$ , then the (1:2) surface complex has local charges of  $-1 \times 2 = -2$  on one side and +2 on the other side. While the (1:1) complex has local charges of -1 and +2, and the extra positive charge is balanced symmetrically by an adsorbed  $\text{X}^-$  ion. It is likely that the more symmetrical charge distribution causes less electrostatic repulsion, and this may explain why  $B_1$  is smaller than  $B_2$ . That  $B_2 > B_1$  for  $\text{Ni}^{2+}$ ,  $\text{Zn}^{2+}$ , and  $\text{Co}^{2+}$  with both  $\text{MnO}_2$  and  $\text{Fe}_2\text{O}_3$  may be owing to less symmetrical charge distributions of the (1:2) surface complexes compared with those of the (1:1) complexes, which cause larger electrostatic repulsion. However, for  $\text{Cu}^{2+}$  with both  $\text{MnO}_2$  and  $\text{Fe}_2\text{O}_3$  and for  $\text{Mn}^{2+}$  with  $\text{MnO}_2$ ,  $B_1 > B_2$ , and for  $\text{Pb}^{2+}$  with  $\text{Fe}_2\text{O}_3$ ,  $B_1 \sim B_2$ . The  $\text{Cu}^{2+}$  and  $\text{Pb}^{2+}$  ions have very high reactivities for adsorption as seen with the  $K_1^\circ$  and  $\beta_2^\circ$  values, and these cations are likely to neutralize the charges of adsorption sites by close and strong contact. If the neutralization is complete, then there is no local charges in the (1:2) complex, while the (1:1) complex has an excess charge of +1. The smaller electric charge of the (1:2) complex may be the cause of the smaller  $B_2$  for  $\text{Cu}^{2+}$ . With some amounts of local charges,  $B_2$  would be about the same as  $B_1$ , and this could explain that  $B_1 \sim B_2$  with  $\text{Pb}^{2+}$ .

**Distribution of M(II) between the solid and solution phases** With the established constants, the fraction of adsorbed metal ions on an oxide for a

given pH, the total concentrations of  $M^{2+}$ ,  $[M^{2+}]_T$ , amounts of the metal oxide, S (surface areas), and solution volume, V, can be computed by solving Eqs. [27]-[30].

The fraction of adsorbed  $M^{2+}$  obtained for a total  $M^{2+}$  concentration of  $10^{-4}$  or  $10^{-6}$  mol dm<sup>-3</sup> and an oxide surface area/solution volume ratio (S/V) of  $80\text{ m}^2\text{ dm}^{-3}$  are plotted against pH for the metal oxide samples (Figs. 16-18). The fraction increases with pH in a sigmoidal manner for all ions and oxides. Figure 16 compares the ability of the metal oxides to adsorb  $Co^{2+}$  ions and the order is:  $MnO_2 > Fe_3O_4 > TiO_2 > Fe_2O_3 > Al_2O_3$ . Figures 17 and 18 compare the affinities of the divalent transition metal ions for  $MnO_2$  and  $Fe_2O_3$ , and the orders are:  $Cu^{2+} > Mn^{2+} > Zn^{2+} > Co^{2+} > Ni^{2+}$  for  $MnO_2$  and  $Pb^{2+} > Cu^{2+} > Zn^{2+} > Co^{2+}$  for  $Fe_2O_3$ .

The above model calculations would enable the selection of the most effective metal oxide, the optimum pH, and metal oxide dose to remove or to recover a specified amount of  $M^{2+}$  ions from a solution, and it appears applicable to water and waste-water treatment technology. The model calculations may further be applied to assess the capacity and ability of soils to retain  $M^{2+}$  ions, which may serve soil fertility evaluations, design of repositories for nuclear waste and heavy metal waste in general, as well as other applications.

#### 4. ION EXCHANGE REACTIONS IN RESINS

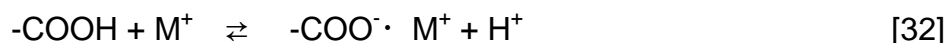
Weak acid type ion exchange resins with carboxyl groups take up alkali metal ions in the resin internal solution by the exchange with carboxyl protons. From the ion exchange behaviors, it has been shown that the resins have sites with different reactivities (polyfunctionality) and that the exchange at a site is suppressed with increasing coverage (Frumkin model [1]) (41, 43, 50). The resins are grouped into gel-types and macroreticular (MR)-types, and there are pores of various sizes within the resins. Both types of resins contain nanopores as the spaces between polymer chains with different sizes depending on the extent of the cross-linking of polymers, and the MR-type resin also contains macropores, voids from where solvent droplets have evaporated. The

polyfunctionality can be ascribed to different pore environments around the ion exchange sites as suggested by Rieman and Walton (88). The reaction mechanism of these resins will now be discussed with the values of model parameters determined.

#### **Measurements of the amounts of alkali metal ions incorporated in resins**

Amberlite IRC-84, a gel type weak acid resin, has a total ion exchange capacity,  $E_c$ , of  $1.0 \times 10^{-2}$  mol g<sup>-1</sup> (89). The resin samples (275-550 mg) were suspended in 200 cm<sup>3</sup> of electrolyte solutions containing 0.5 mol dm<sup>-3</sup> alkali metal nitrate (MNO<sub>3</sub>) at 25°C. The suspensions were stirred, various amounts of 1 mol dm<sup>-3</sup> HNO<sub>3</sub> solution were added, and nitrogen was bubbled through for 3 h to remove dissolved carbon dioxide. Then, 4 cm<sup>3</sup> of 1 mol dm<sup>-3</sup> alkali metal hydroxide (MOH) solution was added to each suspension, and the equilibrium pH was measured when pH showed no change over 3 h. Blank titrations were also carried out for solutions without the resin.

The resin and blank titration curves deviate because of the protons released according to the following ion exchange reaction



Here, a negatively charged carboxyl group in the resin attracts a positively charged metal ion, forming an electrical double layer like the metal oxide/solution interphase. The amount of metal ions M<sup>+</sup> adsorbed was measured from the deviation of the two titration curves by the same principle as that used to determine the amounts of alkali metal and nitrate ions adsorbed or the surface charge on metal oxides (Fig. 3).

Measurements were also carried out for the MR-type weak acid resin, IRC-50, in the same manner.

Figure 19 shows the amount of alkali metal ions M<sup>+</sup> adsorbed per gram of gel-type resin IRC-84, the adsorption density {-COO<sup>-</sup> · M<sup>+</sup>} (mol g<sup>-1</sup>), as a function of pH. It increases with increasing pH because the functional group for ion exchange is a weak acid. In the pH range 4-8, the density increases in the order: Cs<sup>+</sup> < K<sup>+</sup> < Na<sup>+</sup> < Li<sup>+</sup>. A similar affinity series of alkali-metal ions for weak acid cation-exchange resins has been shown by Korkish (90).

The concentration ratio,  $K$ , obtained by applying the mass-action law to reaction [32] and the coverage,  $\theta$ , expressing the extent of the reaction are:

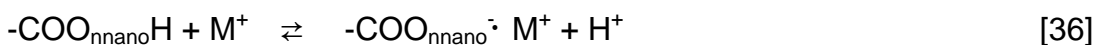
$$K = \{-\text{COO}^-\cdot M^+\}[H^+]/(\{-\text{COOH}\}[M^+]) \quad [33]$$

$$\theta = \{-\text{COO}^-\cdot M^+\}/E_c \quad [34]$$

Figure 20 shows the relationship between  $K$  and  $\theta$  transformed from data in Fig. 19. It is apparent that  $K$  decreases with the progress of the ion exchange reaction  $\theta$  in a complicated manner, suggesting that reactions with different reactivities and suppressions take place simultaneously.

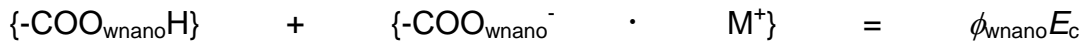
**Stoichiometry** It has been established that, within a gel-type resin, nanopores are developed as the spaces between polymer chains, which appear when the resin swells in aqueous solutions. The pore sizes are less than 2 nm in diameter and different owing to the non-uniform distribution of cross-linking agent in the resin (R. L. Albright, private communication). With increasing cross-linking, less swelling occurs and pore sizes decrease (88). Different nanopore environments around the exchange sites could result in different reactivities (polyfunctionality), because the accessibility of ions to the exchange sites is different depending on the pore size; with increasing cross-linking, ion exchange would become more difficult, especially for ions with larger diameters.

From a stoichiometric point of view, one of the reasons that  $K$  is not constant could be ascribed to ion exchange reactions with different reactivities that occur simultaneously. Two types of carboxyl sites, corresponding to sites on wide and narrow nanopore walls, are considered and termed "w-nano" and "n-nano" site types. It is assumed that the wide nanopores can accommodate hydrated alkali metal ions directly, but that the narrow nanopores require ions to dehydrate before they are able to enter. The ion-exchange reactions of alkali metal ions  $M^+$  with the carboxyl protons at the respective sites can be expressed as



**Material balance** If  $\phi_{\text{wnano}}$  is the fraction of w-nano sites to the total sites, the

material balance equation for the w-nano and n-nano sites are:



[37]



[38]

where the terms in braces express the density of the respective sites in the resin ( $\text{mol g}^{-1}$ ) and  $E_c$  is the ion exchange capacity of the resin ( $\text{mol g}^{-1}$ ).

**Equilibrium conditions** Another reason that  $K$  is not constant can be a suppression of ion exchange with the progress of the reaction. The Frumkin model [1] may be applied to reactions [35] and [36] and the equilibrium conditions are:

$$K_{\text{wnano}}^\circ = \frac{\{-\text{COO}_{\text{wnano}}^-\cdot \text{M}^+\}[\text{H}^+]}{\{-\text{COO}_{\text{wnano}}\text{H}\}[\text{M}^+]} \exp(A_{\text{wnano}} \theta_{\text{wnano}})$$

[39]

$$K_{\text{nnano}}^\circ = \frac{\{-\text{COO}_{\text{nnano}}^-\cdot \text{M}^+\}[\text{H}^+]}{\{-\text{COO}_{\text{nnano}}\text{H}\}[\text{M}^+]} \exp(A_{\text{nnano}} \theta_{\text{nnano}})$$

[40]

where  $K_{\text{wnano}}^\circ$  and  $K_{\text{nnano}}^\circ$  are the "intrinsic" equilibrium constants;  $A_{\text{wnano}}$  and  $A_{\text{nnano}}$  are the lateral interaction constants, being  $A_{\text{wnano}}=r_{\text{wnano}}/(RT)$  and  $A_{\text{nnano}}=r_{\text{nnano}}/(RT)$ ; and  $\theta_{\text{wnano}}$  and  $\theta_{\text{nnano}}$  are the coverages of carboxyl sites with alkali metal ions, being  $\theta_{\text{wnano}} = \{-\text{COO}_{\text{wnano}}^-\cdot \text{M}^+\}/(\phi_{\text{wnano}} E_c)$  and  $\theta_{\text{nnano}} = \{-\text{COO}_{\text{nnano}}^-\cdot \text{M}^+\}/[(1-\phi_{\text{wnano}}) E_c]$ . Here, the coverages are defined with respect to the respective types of sites. The w-nano and n-nano sites are distributed over the different regions of the resin depending on the distribution of the cross-linking agent, and this definition of coverages allows a comparison of the coverages over the respective regions and a comparison of lateral interaction

properties with  $A_{wnano}$  and  $A_{nnano}$ .

**Fitting the model equations to data** According to the model, the measured amount of adsorbed alkali metal ions per gram of resin (density) is the sum of those at the two types of adsorption sites as

$$\{-COO^- \cdot M^+\} = \{-COO_{wnano}^- \cdot M^+\} + \{-COO_{nnano}^- \cdot M^+\} \quad [41]$$

The individual densities at the two types of sites corresponding to the measured overall densities can be calculated from Eqs. [37] - [40], when the values of the five unknown constants are specified as model parameters. The densities calculated with Eq. [41] were compared with the measured densities for all the data to obtain the sum of the squares of the deviations. The parameter values were systematically changed to find the optimum values of the parameters, those that give the least values of the error sum, according to the procedure described elsewhere (41).

The values of the constants obtained by fitting the model and optimizing the model parameters are shown in Table 6. The curves in Figs. 19 and 20 are the calculations with the best fit parameters, and it is seen that the calculated curves reproduce the measured data points well. The fit to the  $K$  values changing over almost four orders of magnitude in a complicated manner is remarkable (41, 43, 50).

**Properties of gel-type resin** Table 6 shows that the values of  $K_{wnano}^\circ$  arrange as:  $Cs^+ \sim K^+ \sim Na^+ < Li^+$  and the values of  $K_{nnano}^\circ$  increase in the order  $Cs^+ < K^+ < Na^+ \sim Li^+$ . These sequences reflect the sequence of the measured amounts of adsorbed ions. The  $K_{wnano}^\circ$  values are more than one order of magnitude larger than the  $K_{nnano}^\circ$  values. The values of  $A_{wnano}$  are about the same for all the alkali metal ions, but  $A_{nnano}$  increases in the order  $Li^+ < Na^+ < K^+ < Cs^+$ ,  $A_{wnano}$  is 5-10 times larger than  $A_{nnano}$ .

The model parameter values determined here can be explained in terms of the different sizes of resin nanopores and ion diameters as assumed in the

model. Ions in aqueous solutions are hydrated and the reported hydrated-ion diameters are: 0.68 nm for  $\text{Li}^+$ , 0.552 nm for  $\text{Na}^+$ , 0.464 nm for  $\text{K}^+$ , and 0.456 nm for  $\text{Cs}^+$  (70). The w-nano sites in wide nanopores (the largest possible diameter is 2 nm as described above) can accommodate hydrated ions directly but the n-nano sites in narrow nanopores require ions to dehydrate before the ions can enter into the pore. Dehydration prior to adsorption requires energy and the  $K_{\text{nnano}}^\circ$  values are smaller than the  $K_{\text{wnano}}^\circ$  values. This is an energetic, thermodynamic difficulty for ions entering into small pores and not a kinetic difficulty.

The differences in  $\phi_{\text{wnano}}$  values can be explained by the different diameters of ions. The lithium ion in water  $\text{Li}^+(\text{aq})$  has the largest hydrated-ion diameter among the alkali metal ions as described above and the fraction of w-nano sites,  $\phi_{\text{wnano}}$ , for  $\text{Li}^+(\text{aq})$  is therefore the smallest. The similar  $\phi_{\text{wnano}}$  values for  $\text{Na}^+$ ,  $\text{K}^+$ , and  $\text{Cs}^+$  ions are likely to be due to the similar hydrated-ion diameters of these ions.

The  $K_{\text{wnano}}^\circ$  values, a measure of the interaction between the hydrated cation and the negatively charged site, are very similar (max. 2 times difference), and this can be explained with the hydrated-ion diameters of alkali metal ions without large differences (max. 1.4 times difference). Among the hydrated alkali metal ions, however, the  $\text{Li}^+$  ion, with the largest hydrated-ion diameter and hence the smallest charge density, shows the largest  $K_{\text{wnano}}^\circ$  value. This is contrary to the expectation from the electric charge density on the hydrated cations, suggesting the interaction not to be simply electrostatic. There seems to be some contribution of coordination-type bonds to the adsorption of hydrated  $\text{Li}^+$  ions on the sites in wide nanopores, as  $\text{Li}^+$  ions in solution form more stable EDTA complexes than  $\text{Na}^+$  ions (91).

On the other hand, larger differences are seen in the  $K_{\text{nnano}}^\circ$  values. The reported crystallographic diameters of alkali metal ions are: 0.120 nm for  $\text{Li}^+$ , 0.190 nm for  $\text{Na}^+$ , 0.266 nm for  $\text{K}^+$ , and 0.338 nm for  $\text{Cs}^+$  (70), and the smaller

the crystallographic diameters (3 times difference), the larger the  $K_{nnano}^\circ$  values (4 times difference). Then, at the n-nano sites the electrostatic interaction between the dehydrated cation and the negatively charged site changes significantly according to the electric charge density determined by the crystallographic diameters of the dehydrated ions.

The values of the lateral interaction parameter,  $A$ , can also be explained by the size and hydrated state of the adsorbed ions. That  $A_{wnano}$  is larger than  $A_{nnano}$  indicates that lateral interactions at the w-nano sites are larger than those at the n-nano sites. The positive charge of cations at a w-nano site is shielded from the negative charge of sites by hydrated water molecules, while at an n-nano site dehydrated cations are directly in contact with the negative sites. The adsorbed hydrated cation-site pairs are likely to have a large polarization, leading to a strong repulsive interaction with other pairs. However, the adsorbed dehydrated cation-site pairs would be less polarized due to direct contact, resulting in only a weak interaction with other pairs, and hence  $A_{wnano} > A_{nnano}$ . The very similar  $A_{wnano}$  values for the hydrated alkali metal ions can be ascribed to their similar diameters like the consideration above for the similar  $K_{wnano}^\circ$  values. The increase in the sequence of the  $A_{nnano}$  values coincides with the increasing crystallographic diameter of the ions. For a dehydrated cation with a large diameter, the neutralization of its charge by the negative site is incomplete, polarization remains, and repulsive interactions with neighboring ion-site pairs would be large.

**Properties of MR-type resin** A similar evaluation of the ion exchange properties was made for another MR-type weak acid resin, IRC-50 (50). The MR-type resin includes macropores with average diameters of several *tens* to several *hundreds* nm which are voids from where solvent droplets have evaporated (92). The MR-type resins also have nanopores, the spaces between polymer chains (< 2 nm), as found for the gel-type weak acid resin IRC-84. It can then be expected that there are three types of sites with different reactivities: "macro" sites on macropore walls, "w-nano" sites on wide nanopore walls, and "n-nano" sites on narrow nanopore walls as illustrated in Fig. 21. The

ion-exchange data with the IRC-50 are due to the reactions occurring simultaneously at the sites in these pores, but the reaction at the narrow nanopores was disregarded as will be explained next. Among these pores, the narrow nanopores are smaller than the hydrated-ion diameters, and ions in solution must dehydrate before they can react with the sites in the narrow nanopores. The reactivity here is therefore smaller than that in the other two kinds of pores because of the requirement for dehydration energy, and the contribution of this reaction to the overall reaction is small. When analyzing the overall ion-exchange data, it is difficult to obtain reliable model parameter values for less contributing reactions, and this is the reason why the reaction in the narrow nanopores is disregarded.

The intrinsic equilibrium constant for the w-nano sites is  $K_{wnano}^\circ$  and the lateral interaction constant is  $A_{wnano}$ , similar to IRC-84. The intrinsic equilibrium constant for the sites in the macropore is defined as  $K_{macro}^\circ$ , the lateral interaction constant as  $A_{macro}$ , and the fraction of macro sites to the sum of the number of macro and w-nano sites as  $\phi_{macro}$ . The model parameter values determined for the macro and w-nano sites of IRC-50 are listed in Table 7.

The  $K_{macro}^\circ$  value decreases with increasing atomic number of the ions. The  $K_{wnano}^\circ$  value also decreases from  $\text{Li}^+$  to  $\text{K}^+$ , but  $\text{Cs}^+$  shows about the same  $K_{macro}^\circ$  value as  $\text{Li}^+$ . The  $A_{macro}$  value for  $\text{Li}^+$  is smaller than the other three ions. The  $A_{wnano}$  values are about the same for all the four ions. The  $\phi_{macro}$  values are also very similar for these ions, but  $\text{Cs}^+$  is slightly smaller than the other three ions. As a whole, the ion exchange reactivities ( $K_{macro}^\circ$  and  $K_{wnano}^\circ$ ) are about the same for the two types of sites, but the repulsive lateral interaction at the w-nano sites ( $A_{wnano}$ ) is larger than at the macro sites ( $A_{macro}$ ). The fraction of the macro sites  $\phi_{macro}$  shows that this site type comprises about 70% irrespective of the kind of ion.

These differences in the parameter values can be interpreted in terms of the pore and ion sizes. The macropores and wide nanopores have diameters large enough to accommodate hydrated ions, the ions adsorbed to the negatively charged sites on these pore walls would be both hydrated alkali metal ions, and  $K_{\text{macro}}^\circ$  and  $K_{\text{wnano}}^\circ$  are similar. However, due to the very different pore diameters of the macro and wide nanopores, the across-pore interaction mentioned above for hydroxyl sites on metal oxides and for n-nano carbosyl sites in resin nanopores would be different at the two types of sites. The size of wide nanopores is only several times larger than the hydrated ions, and repulsive interactions from ions adsorbed on opposite pore walls (across-pore interaction) in wide nanopores may be more significant than in macropores, and this could explain why  $A_{\text{macro}} < A_{\text{wnano}}$ .

A comparison of the properties of the two resins can be made with the model parameters. The  $A_{\text{wnano}}$  values of IRC-84 (Table 6) coincide with those of IRC-50 (Table 7), suggesting that the wide nanopore environments around the sites of these resins are very similar. The  $K_{\text{wnano}}^\circ$  values at both the w-nano sites are however different for the two resins; the values of IRC-84 are more than two orders of magnitude larger than those of IRC-50. This difference may arise as IRC-84 is an acrylic acid resin  $[(-R)_2C(H)COOH]$  and IRC-50 a metacrylic acid resin  $[(-R)_2C(CH_3)COOH]$  (89). The methyl group of IRC-50 exerts an electron repelling effect and would reduce the acid dissociation strength of the carboxyl group, as Rohm & Haas reported that IRC-50 is a weaker acid than IRC-84 (89).

Three types of pores of the weak acid ion-exchange resins, macropores, wide nanopores, and narrow nanopores, have been characterized in this investigation. The macropores and wide nanopores can be distinguished only by the different lateral interaction properties they give rise to, possibly due to different across-pore interactions. The intrinsic reactivities of the sites in these pores are the same, the reacting species are likely to be hydrated ions in both, and the fraction of macropore sites  $\phi_{\text{macro}}$  is independent of the hydrated-ion diameters of entering ions. However, the distinction between the wide

nanopores and narrow nanopores arises from the hydrated diameters of entering ions; with decreasing hydrated-ion diameter the fraction of wide nanopore sites to the total nanopore sites  $\phi_{\text{wnano}}$  increases. The overall reactivity of sites in narrow nanopores, including the dehydration reactions, is very low, but the lateral interactions here are small possibly due to the small polarization of the dehydrated cation and negatively charged site pair.

To substantiate the resin pore structure discussed above, porosimetry analysis may be applied. Resin nanopores are the spaces between polymer chains, and the spaces are too narrow for gas molecules and mercury atoms to enter into. As a result, porosimetry cannot be applied to the nanopores. Macropores, voids from where solvent droplets have evaporated, may be analyzed by porosimetry, and the IRC-50 manufacturer reports that the porosity of IRC-50 is  $0.152 \text{ cm}^3 \text{ g}^{-1}$  and that the average pore diameter is 70-400 nm (89). Porosimetry gives reliable results for macropores with diameters larger than several tens nm, but there could also be macropores with diameters smaller than that limit. The pore diameter critical to the across-pore interaction (coulombic repulsion between ions adsorbed on opposite pore walls) would be 10 nm or so, and the macropores assigned in this investigation as those showing no across-pore interaction would include very small macropores ( $\phi > 10 \text{ nm}$ ) undetectable by porosimetry. Much smaller macropores ( $2 < \phi < 10 \text{ nm}$ ) showing across-pore interaction would be classified as wide nanopores in this investigation. A direct comparison of our results with the porosimetry data is difficult.

In this paper, the pores in ion-exchange resins are classified as nanopores (narrow and wide) and macropores. The nanopores correspond to the micropores ( $\phi < 2 \text{ nm}$ ) by IUPAC terminology. The reason why the IUPAC terminology was not followed in this paper is: the IUPAC micropores have dimensions in the nm and sub-nm orders, but micro- could give an impression of  $\mu\text{m}$  order sizes. Recently, work in nm dimensions is developing with nano- as a common keyword, and the term nanopores looked just right to name pores with nanometer sizes. Also, the macropores in this paper include the IUPAC mesopores ( $2 < \phi < 50 \text{ nm}$ ) and macropores ( $\phi > 50 \text{ nm}$ ), as the modeling approach in this paper does not distinguish between mesopores and

macropores.

## 5. ACTIVITY COEFFICIENTS OF INTERPHASE SPECIES

Summarizing the discussion so far, this paper has shown that the intrinsic equilibrium constants for ion exchange reactions on metal oxides and resins are expressed with the concentrations (densities) of the relevant species and an exponential term containing the surface coverage  $\theta$  (Frumkin equation). Equilibrium constants are defined with activities, and the Frumkin equation can be considered from an activity point of view. For a monovalent cation exchange reaction on acid hydroxyl sites [5], the equilibrium constant  $K_a^\circ$  in Eq. [18] may be defined with the activities of relevant species as

$$K_a^\circ = K_a \frac{y(-O^- \cdot M^+) y(H^+)}{y(-OH(a)) y(M^+)} \quad [42]$$

where  $K_a$  is the concentration ratio and  $y$  is the activity coefficient of each species. The exponential term in Eq. [18] is then equated to the activity coefficient ratio as

$$\exp(A_a \theta_a) = \frac{y(-O^- \cdot M^+) y(H^+)}{y(-OH(a)) y(M^+)} \quad [43]$$

Here, the ratio  $y(H^+)/y(M^+)$  is 1 or a constant close to 1 since the ionic strength of the solution is kept constant with  $MNO_3$ . It is apparent that the exponential function expressing the suppression of ion exchange is then determined practically by the activity coefficient ratio of the interphase species

$$y(-O^- \cdot M^+)/y(-OH(a)).$$

The activity coefficients of interphase species may be formulated in the following way as was done for ICR-84 (44):

$$y(-O^- \cdot M^+) = \exp(\alpha_a \theta_a) \quad [44]$$

$$y(-OH(a)) = \exp(-\beta_a \theta_a) \quad [45]$$

Here  $\alpha_a$  and  $\beta_a$  are constants and  $\theta_a$  is the surface coverage.

When the surface coverage at the acid hydroxyl sites is so low that the  $\alpha_a \theta_a$  term in Eq. [44] can be regarded as 0, the activity coefficient  $y(-O^- \cdot M^+)$  is 1. However, with the progress of a reaction and hence with increasing  $\theta_a$ ,  $y(-O^- \cdot M^+)$  becomes larger than 1. Figure 22 illustrates schematically the change in  $y(-O^- \cdot M^+)$  as a function of surface coverage  $\theta_a$ . This can be explained by  $-O^- \cdot M^+$  pairs repelling each other electrostatically and geometrically (Fig. 4). In Eq. [45],  $y(-OH(a))$  decreases with increasing  $\theta_a$  with the progress of the reaction (Fig. 22). This may be because it becomes difficult for the hydroxyl protons to leave the oxide owing to electrostatic attraction by neighboring negatively charged sites (Fig. 4). Further quantitative considerations on interactions between interphase species on the molecular level would allow a purely theoretical derivation of Eqs. [44] and [45].

The increase in  $y(-O^- \cdot M^+)$  results in a decrease in the concentration ratio  $K_a$  in Eq. [42] as  $K_a^\circ$  is constant. The concomitant decrease in  $y(-OH(a))$  with  $\theta_a$  also results in a decrease in the concentration ratio  $K_a$ . Therefore, with the progress of a reaction, both  $y(-O^- \cdot M^+)$  and  $y(-OH(a))$  cooperate to decrease the concentration ratio  $K_a$ , and the decrease in the concentration ratio indicates the suppression of a reaction. Consequently, the assumption in the Frumkin equation that "the Gibbs free energy change  $\Delta G$  increases linearly with coverage resulting in the suppression of a reaction" has been interpreted in terms of changes in the activity coefficients of the respective interphase species with coverage. The suppressive lateral interaction constant  $A_a$  is thus

$$A_a = \alpha_a + \beta_a \quad [46]$$

The constant  $\alpha_a$  may be regarded to represent the properties of adsorbed ions repelling each other and  $\beta_a$  the properties of exchanger protons of the functional groups to be fixed to the exchangers by neighboring negatively charged sites,

but a determination of individual values of  $\alpha_a$  and  $\beta_a$  is difficult. In this investigation, the properties of ions and exchangers have been evaluated with the values of a lateral interaction constant  $A_a$ . This can be justified as: when the properties of ions are examined with the same exchanger,  $\beta_a$  remains constant and  $A_a$  reflects  $\alpha_a$ , and for the evaluation of exchanger properties with the same ions,  $A_a$  reflects  $\beta_a$ .

In the discussion above, the effect of  $\text{-OH}_2^+ \cdot \text{NO}_3^-$ , an ion exchange product at base hydroxyl sites, on the activities of  $\text{-O}^- \cdot \text{M}^+$  and  $\text{-OH(a)}$  was ignored. This is because the pH dependencies of reactions at acid and base sites are opposite, and when one reaction is dominant, the other reaction is minor. As a result, only the effect of the ion exchange product from a reaction of interest is considered.

The activity coefficient  $y$  of ions in solution is well described by the following Debye-Hückel equation (93):

$$y = \exp\left(-\frac{AZ^2\sqrt{I}}{1+Ba\sqrt{I}}\right)$$

[47]

where  $A$  and  $B$  are constants,  $Z$  the valence of the ions,  $a$  the hydrated-ion diameter of ions, and  $I$  the ionic strength of the solution. This equation considers the effect of electrostatic attraction between ions with opposite charges on the ion activity. When the ion concentration is low ( $I \sim 0$ ), these ions behave independently and the ion activity is equal to the ion concentration, i.e.,  $y=1$ . However, with increasing ionic strength  $I$ , there is electrostatic attraction between ions with opposite charges, then the ion activity becomes smaller than the concentration, and as a result  $y$  becomes smaller than 1. The interaction between ions with charges of the same sign are not considered, because these ions repel each other and migrate to areas where there is no interaction. The activity coefficient of neutral species in solution is taken as 1 because of the absence of electrostatic interaction with other ions.

A comparison of Eqs. [44] and [45] with Eq. [47] indicates the characteristics of the two activity coefficients of interphase species and of solution species. The

coverage  $\theta$  at the interphase corresponds to the ionic strength  $I$  of the solution. The electrical and geometrical ion atmosphere in the 2-D interphase could be expressed by the surface coverage  $\theta$ , just as the ionic atmosphere in the 3-D solution phase is expressed by the ionic strength  $I$ . However, very different features were pointed out above for the activity coefficients of interphase species. For a surface ion pair  $-O^- \cdot M^+$ , the repulsive interaction between them plays a role in determining their activity, but for ions in solution such a repulsive interaction is not important. For a neutral interphase species  $-OH(a)$ , the electric attraction between the hydroxyl proton and neighboring negatively charged sites determines the activity coefficient of  $-OH(a)$ , but there is no such electric interaction with a neutral species in solution. These differences could arise from the different existing states of interphase species and of solution species; immobile interphase species confined to the 2-D phase are subject to both repulsive and attractive lateral interactions, while species in the 3-D solution phase move to minimize repulsive interactions.

For the other ion exchange reactions, with monovalent cations and an anion on metal oxides and on resins and divalent metal ions on metal oxides, similar considerations apply to the activity coefficients of the other interphase species.

## ACKNOWLEDGMENTS

This work was supported by a grant-in-aid for Scientific Research from the Ministry of Education, Culture, Sports, Science and Technology, Japan (14580580).

## REFERENCES

- [1] W. Rieman, III, H. F. Walton, Ion Exchange in Analytical Chemistry, Pergamon, Oxford, 1970, pp. 1-2.
- [2] D. G. Kinniburgh, M. L. Jackson, in: M. A. Anderson, A. J. Rubin (Eds.), Adsorption of Inorganics at Solid-Liquid Interfaces, Ann Arbor Science, Ann Arbor, MI, 1981, p. 117.
- [3] C. E. Harland, Ion Exchange: Theory and Practice, 2nd Ed., Royal Society of Chemistry, Cambridge, 1994, pp. 101-104.
- [4] W. Rieman, III, H. F. Walton, Ion Exchange in Analytical Chemistry, Pergamon, Oxford, 1970, p. 42.
- [5] J. Westall, H. A. Hohl, *Adv. Colloid Interface Sci.* **12** (1980) 265.
- [6] P. W. Schindler, in: M. A. Anderson, A. J. Rubin (Eds.), Adsorption of Inorganics at Solid-Liquid Interfaces, Ann Arbor Science, Ann Arbor, MI, 1981, pp. 1-49.
- [7] F. M. M. Morel, J. G. Yeasted, J. C. Westall, in: M. A. Anderson, A. J. Rubin (Eds.), Adsorption of Inorganics at Solid-Liquid Interfaces, Ann Arbor Science, Ann Arbor, MI, 1981, pp. 263-294.
- [8] R. O. James, G. A. Parks, in: E. Matijević (Ed.), Surface and Colloid Science, Vol. 12, Plenum, New York, 1982, pp. 119-216.
- [9] J. C. Westall, in: J. A. Davis, K. F. Hayes (Eds.), Geochemical Processes at Mineral Surfaces, ACS Symposium Ser. 323, American Chemical Society, Washington, DC, 1986, pp. 54-78.
- [10] K. F. Hayes, J. O. Leckie, in: J. A. Davis, K. F. Hayes (Eds.), Geochemical Processes at Mineral Surfaces, ACS Symposium Ser. 323, American Chemical Society, Washington, DC, 1986, pp. 114-141.
- [11] J. C. Westall, in: W. Stumm (Ed.), Aquatic Surface Chemistry, John Wiley & Sons, New York, 1987, pp. 3-32.
- [12] G. Sposito, The Chemistry of Soils, Oxford University Press, New York, 1989, pp. 160-165.
- [13] D. A. Dzombak, F. M. M. Morel, Surface Complexation Modeling, John Wiley & Sons, New York, 1990, pp. 9-41.
- [14] J. A. Davis, D. B. Kent, in: M. F. Hochella, Jr., A. F. White (Eds.), Reviews

in Mineralogy, Vol. 23, Mineralogical Society of America, Washington, DC, 1990, pp. 204-230.

- [15] K. F. Hayes, G. Redden, W. Ela, J. O. Leckie, *J. Colloid Interface Sci.* **142** (1991) 448.
- [16] W. Stumm, Chemistry of the Solid-Water Interface, John Wiley & Sons, New York, 1992, pp. 67-78.
- [17] S. Goldberg, *Adv. Agron.* **47** (1992) 233.
- [18] D. L. Sparks, Environmental Soil Chemistry, Academic Press, San Diego, 1995, pp. 119-127.
- [19] J. J. Morgan, W. Stumm, Aquatic Chemistry, 3rd Ed., John Wiley & Sons, New York, 1996, pp. 557-574.
- [20] J. I. Drever, The Geochemistry of Natural Waters, 3rd Ed., Prentice Hall, Upper Saddle River, NJ, 1997, pp. 87-105.
- [21] U. Singh, G. Uehara, in: D. L. Sparks (Ed.), Soil Physical Chemistry, 2nd Ed., CRC, Boca Raton, FL, 1999, pp. 1-46.
- [22] J. M. Zachara, J. C. Westall, in: D. L. Sparks (Ed.) Soil Physical Chemistry, 2nd Ed., CRC, Boca Raton, FL, 1999, pp. 47-95.
- [23] A. Kozawa, *Prog. Batteries Solar Cells* **7** (1988) 327.
- [24] R. O. James, G. A. Parks, in: E. Matijević (Ed.), Surface and Colloid Science, Vol. 12, Plenum, New York, 1982, p. 134.
- [25] J. A. Davis, D. B. Kent, in: M. F. Hochella, Jr., A. F. White (Eds.), Reviews in Mineralogy, Vol. 23, Mineralogical Society of America, Washington, DC, 1990, p. 190.
- [26] X. Jin, J. Talbot, N.-H. L. Wang,, *AIChE J.* **40** (1994) 1685.
- [27] H.-J. Ulrich, W. Stumm, *Environ. Sci. Technol.* **22** (1988) 37.
- [28] H. Tamura, in: A. Hubbard (Ed.), Encyclopedia of Surface and Colloid Science, Marcel Dekker, New York, 2002, pp. 2856-2875.
- [29] E. Gileadi, E. Kirowa-Eisner, J. Penciner, *Interfacial Electrochemistry*, Addison-Wesley, Reading, MA, 1975, pp. 82-83.
- [30] W. Stumm, Chemistry of the Solid-Water Interface, John Wiley & Sons, New York, 1992, pp. 93-94.

- [31] J. O'M. Bockris, S. U. M. Khan, *Surface Electrochemistry*, Plenum, New York, 1993, p. 263.
- [32] J. J. Morgan, W. Stumm, *Aquatic Chemistry*, 3rd Ed., John Wiley & Sons, New York, 1996, p. 526.
- [33] W. Stumm, *Chemistry of the Solid-Water Interface*, John Wiley & Sons, New York, 1992, p. 97.
- [34] L. H. Allen, E. Matijević, L. Meites, *J. Inorg. Nucl. Chem.* **33** (1971) 1293.
- [35] H. Tamura, E. Matijević, L. Meites, *J. Colloid Interface Sci.* **92** (1983) 303.
- [36] H. Tamura, N. Katayama, R. Furuichi, *Bunseki Kagaku* **37** (1988) 395.
- [37] H. Tamura, T. Oda, M. Nagayama, R. Furuichi, *J. Electrochem. Soc.* **136** (1989) 2782.
- [38] H. Tamura, T. Tatsumi, R. Furuichi, *Hyomen Gijyutsu* **40** (1989) 1116.
- [39] N. Katayama, H. Tamura, R. Furuichi, *Bunseki Kagaku* **39** (1990) 547.
- [40] H. Tamura, R. Furuichi, *Bunseki Kagaku* **40** (1991) 635.
- [41] H. Tamura, T. Oda, R. Furuichi, *Anal. Chim. Acta* **244** (1991) 275.
- [42] N. Katayama, H. Tamura, R. Furuichi, *Denki Kagaku* **60** (1992) 887.
- [43] H. Tamura, M. Kudo, R. Furuichi, *Anal. Chim. Acta* **271** (1993) 305.
- [44] H. Tamura, N. Katayama, R. Furuichi, *Bunseki Kagaku* **42** (1993) 715.
- [45] H. Tamura, K. Ohkita, N. Katayama, R. Furuichi, *Bunseki Kagaku* **43** (1994) 831.
- [46] N. Katayama, S. Tamura, H. Tamura, R. Furuichi, *Denki Kagaku* **62** (1994) 251.
- [47] H. Tamura, N. Katayama, R. Furuichi, *Environ. Sci. Technol.* **30** (1996) 1198.
- [48] H. Tamura, N. Katayama, R. Furuichi, *J. Colloid Interface Sci.* **195** (1997) 192.
- [49] H. Tamura, R. Furuichi, *J. Colloid Interface Sci.* **195** (1997) 241.
- [50] H. Tamura, M. Kudo, R. Furuichi, *Reactive & Functional Polymers* **38** (1998) 177.
- [51] S. Pivovarov, *J. Colloid Interface Sci.* **206** (1998) 122.
- [52] D. G. Kinniburgh, *Environ. Sci. Technol.* **20** (1986) 895.
- [53] E. Höglfeld, *Reactive Polymers* **11** (1989) 199.

- [54] C.-H. Yang, *J. Colloid Interface Sci.* **208** (1998) 379.
- [55] O. Altin, Ö. Özbelge, T. Dogu, *J. Colloid Interface Sci.* **198** (1998) 130.
- [56] E. A. Jenne, in: R. A. Baker (Ed.), *Trace Inorganics in Water*, *Adv. Chem.* Ser. No. 73, American Chemical Society, Washington, DC, 1968, p. 337.
- [57] J. S. Reed, *Principles of Ceramics Processing*, 2nd Ed., John Wiley & Sons, New York, 1995, p. 150.
- [58] H. Tamura, A. Tanaka, K. Mita, R. Furuichi, *J. Colloid Interface Sci.* **209** (1999) 225.
- [59] H. Tamura, K. Mita, A. Tanaka, M. Ito, *J. Colloid Interface Sci.* **243** (2001) 202.
- [60] H. P. Boehm, *Discuss. Faraday Soc.* **52** (1971) 264.
- [61] J. N. Mukherjee, *J. Indian Chem. Soc.* **2** (1925) 191.
- [62] B. Ghosh, *J. Chem. Soc.* **1926** (1926) 2605.
- [63] B. N. Ghosh, S. N. Chakravarty, M. L. Kundu, *J. Indian Chem. Soc.* **28** (1951) 319.
- [64] J. W. Murray, *J. Colloid Interface Sci.* **46** (1974) 357.
- [65] W. Stumm, *Chemistry of the Solid-Water Interface*, John Wiley & Sons, New York, 1992, pp. 15-18.
- [66] L. Meites, *CRC Crit. Rev. Anal. Chem.* **8** (1979) 1.
- [67] J. F. Rusling, T. F. Kumasinski, *Nonlinear Computer Modeling of Chemical and Biochemical Data*, Academic Press, San Diego, 1996.
- [68] K. Yamaoka, *Yakubutsu Tainaidotai Kaisekiho*, Nankodo, Tokyo, 1984, pp. 124-125.
- [69] K. Tanaka, *J. Catalysis* **8** (1967) 1.
- [70] F. A. Cotton, G. Wilkinson, *Advanced Inorganic Chemistry*, 2nd Ed., Interscience, New York, 1966, p. 422.
- [71] C. B. Amphlett, *Inorganic Ion Exchangers*, Elsevier, Amsterdam, 1964, p. 21.
- [72] P. A. O'Day, G. E. Brown, Jr., G. A. Parks, *J. Colloid Interface Sci.* **165** (1994) 269.
- [73] P. A. O'Day, G. A. Parks, G. E. Brown, Jr., *Clays Clay Minerals* **42** (1994) 337.
- [74] S. N. Towle, J. R. Bargar, G. E. Brown, Jr., G. A. Parks, *J. Colloid Interface*

Sci. **187** (1997) 62.

- [75] S.-F. Cheah, G. E. Brown, Jr., G. A. Parks, J. Colloid Interface Sci. **208** (1998) 110.
- [76] T. P. Trainor, G. E. Brown, Jr., G. A. Parks, J. Colloid Interface Sci. **231** (2000) 359.
77. D. G. Kinniburgh, J. Soil Sci. **34** (1983) 759.
- [78] B. D. Honeyman, J. O. Leckie, in: J. A. Davis, K. F. Hayes (Eds.), Geochemical Processes at Mineral Surfaces, ACS Symposium Ser. 323, American Chemical Society, Washington, DC, 1986, p. 163.
- [79] B. Müller, L. Sigg, J. Colloid Interface Sci. **148** (1992) 517.
- [80] R. O. James, T. W. Healy, J. Colloid Interface Sci. **40** (1972) 53.
- [81] J. W. Murray, Geochim. Cosmochim. Acta **39** (1975) 635.
- [82] P. Loganathan, R. G. Burau, D. W. Fuerstenau, Soil Sci. Am. J. **41** (1977) 57.
- [83] W. Stumm, Chemistry of the Solid-Water Interface, John Wiley & Sons, New York, 1992, p. 27.
- [84] The Hokkaido Section of the Japan Society for Analytical Chemistry, Bunseki Kagaku Hanno no Kiso, Baifukan, Tokyo, 1980, p. 262.
- [85] P. W. Schindler, B. Fürst, R. Dick, P. Wolf, J. Colloid Interface Sci. **55** (1976) 469.
- [86] D. A. Dzombak, F. M. M. Morel, Surface Complexation Modeling, John Wiley & Sons, New York, 1990, pp. 299-315.
- [87] F. Basolo, R. G. Pearson, Mechanisms of Inorganic Reactions, 2nd Ed., John Wiley & Sons, New York, 1967, pp. 80-89.
- [88] W. Rieman, III, H. F. Walton, Ion Exchange in Analytical Chemistry, Pergamon, Oxford, 1970, pp. 13-14.
- [89] Technical bulletin from Rohm & Haas (Leaflet from Organo Co., Japan).
- [90] J. Korkish, Handbook of Ion Exchange Resins: Their Application to Inorganic Analytical Chemistry, Vol. 1, CRC Press, Boca Raton, 1989, p. 16.
- [91] G. Schwarzenbach, H. Ackerman, Helv. Chim. Acta. **30** (1947) 1798.
- [92] M. Senoo, M. Abe, T. Suzuki, Ion Kokan, Kodansha, Tokyo, 1991, p. 33.
- [93] J. J. Morgan, W. Stumm, Aquatic Chemistry, 3rd Ed., John Wiley & Sons, New York, 1996, p. 103.

Figure legend

Fig. 1 Apparatus for the determination of the amount of surface hydroxyl groups on metal oxides by the Grignard method

1. reaction flask, 2. constant temperature water bath, 3. spoon, 4. CH<sub>4</sub> gas cylinder, 5. magnetic stirrer, 6. dry ice trap, 7. pump to circulate the constant temperature water, 8. three direction valve, 9. gas burette, 10. NaCl saturated solution

Ref. 58

Fig. 2 Hydration and hydroxylation of metal oxide surfaces with the formation of (a) acid hydroxyl groups and (b) base hydroxyl groups

lattice oxide ion (○), lattice metal ion (●)

Ref. 28

Fig. 3 Schematic titration curves for (A) metal oxide suspension and (B) blank solution

Ref. 47

Fig. 4 Model of electrical double layers

Fig. 5 Surface charge density  $\sigma$  vs. pH for metal oxides at ionic strength 0.1 M (NaNO<sub>3</sub>) and 25°C

$\text{MnO}_2\text{-IC1}$  ( $\circ$ ),  $\text{MnO}_2\text{-IC12}$  ( $\square$ ),  $\text{MnO}_2\text{-IC22}$  ( $\bullet$ ),

$\text{TiO}_2$  ( $\triangle$ ),  $\text{Fe}_3\text{O}_4$  ( $\blacktriangle$ ),  $\text{Fe}_2\text{O}_3$  ( $\Phi$ ),  $\text{Al}_2\text{O}_3$  ( $\blacksquare$ )

Points, experimental; curves, calculated

Ref. 28

Fig. 6 Surface charge density  $\sigma$  vs. pH for  $\text{MnO}_2\text{-IC12}$  with different alkali metal ions ( $M^+$ ) at ionic strength 0.1 M ( $\text{MNO}_3$ ) and 25°C

$\text{Li}^+$  ( $\circ$ ),  $\text{Na}^+$  ( $\square$ ),  $\text{K}^+$  ( $\triangle$ ),  $\text{Cs}^+$  ( $\bullet$ )

Ref. 47

Fig. 7 Plot of  $\log K_a$  against  $\theta_a$  for  $\text{MnO}_2\text{-IC12}$  with different alkali metal ions ( $M^+$ ) at ionic strength 0.1 M ( $\text{MNO}_3$ ) and 25°C

$\text{Li}^+$  ( $\circ$ ),  $\text{Na}^+$  ( $\square$ ),  $\text{K}^+$  ( $\triangle$ ),  $\text{Cs}^+$  ( $\bullet$ )

Ref. 47

Fig. 8 Relationship between  $\log K_a^\circ$  or  $\log K_b^\circ$  and electronegativity  $X_i$  of lattice metal ions

$K_a^\circ$  ( $\circ$ ),  $K_b^\circ$  ( $\bullet$ )

Ref. 28

Fig. 9 Lateral interactions between  $\text{Na}^+$  ions adsorbed on outer and inner surfaces

(a) flat outer surface, (b) inner surface of tunnel-like pore, (c) inner surface of closed pore

Ref. 58

Fig. 10 Calculation of site density vs. pH for  $\text{Fe}_3\text{O}_4$  at ionic strength 0.1 M ( $\text{NaNO}_3$ ) and 25°C

Ref . 47

Fig. 11 Adsorption isotherm for  $\text{Co}^{2+}$  on  $\text{Fe}_3\text{O}_4$  with different pH at ionic strength 0.1 M ( $\text{NaNO}_3$ ) and 25°C

Points, experimental; curves, calculated

Ref. 48

Fig. 12  $\log K_1^\circ$  and  $\log \beta_2^\circ$  vs. electronegativity  $X_i$  of lattice metal ions

$K_1^\circ$  (○),  $\beta_2^\circ$  (●)

Ref. 48

Fig. 13  $\log K_1^{\circ*}$  (bottom) and  $\log \beta_2^{\circ*}$  (top) vs. electronegativity  $X_i$  of lattice metal ions

Fig. 14 Correlation between stability constants of surface complexes  $K_1^\circ$  and

hydroxo complexes  $K_1^{\text{OH}}$

Ref. 49

Fig. 15 Model of (1:1) and (1:2) surface complexes of divalent heavy metal ions,  $M^{2+}$ , formed by exchange with protons of acid-type surface hydroxyl groups on metal oxide, -OH(a), in the presence of a monovalent anion,  $X^-$

Ref. 48

Fig. 16 Calculated fractions of adsorbed  $\text{Co}^{2+}$  on metal oxides as a function of pH for an initial  $\text{Co}^{2+}$  concentration of  $10^{-4}$  M and an oxide surface area S/solution volume V ratio of  $80 \text{ m}^2 \text{ dm}^{-3}$  at ionic strength 0.1 M ( $\text{NaNO}_3$ ) and  $25^\circ\text{C}$

Ref. 48

Fig. 17 Calculated fractions of adsorbed  $M^{2+}$  on  $\text{MnO}_2$  as a function of pH for an initial  $M^{2+}$  concentration of  $10^{-4}$  M and an oxide surface area S/solution volume V ratio of  $80 \text{ m}^2 \text{ dm}^{-3}$  at ionic strength 0.1 M ( $\text{NaNO}_3$ ) and  $25^\circ\text{C}$

Ref. 49

Fig. 18 Calculated fractions of adsorbed  $M^{2+}$  on  $\text{Fe}_2\text{O}_3$  as a function of pH for an initial  $M^{2+}$  concentration of  $10^{-6}$  M and an oxide surface area S/solution volume V ratio of  $80 \text{ m}^2 \text{ dm}^{-3}$  at ionic strength 0.1 M ( $\text{NaNO}_3$ ) and  $25^\circ\text{C}$

Ref. 49

Fig. 19 Adsorption density of alkali metal ions,  $M^+$ , on IRC-84 vs. pH for ionic strength 0.5 M ( $\text{MNO}_3$ ) at  $25^\circ\text{C}$

$\text{Li}^+$  (○),  $\text{Na}^+$  (△),  $\text{K}^+$  (□),  $\text{Cs}^+$  (○)

Points, experimental; curves, calculated

Ref. 43

Fig. 20 Apparent concentration ratio,  $K$ , of IRC-84 vs. apparent coverage,  $\theta$ , for ionic strength 0.5 M ( $MNO_3$ ) at 25°C

$Li^+$  (○),  $Na^+$  (△),  $K^+$  (□),  $Cs^+$  (○)

Points, experimental; curves, calculated

Ref. 50

Fig. 21 Model of macro- and nanopores in resins

Fig. 22 Activity coefficients of interphase species  $\gamma$  vs.  $\theta$

**Table 1** Specific surface areas  $S_{\text{BET}}$  and hydroxyl site densities  $N_s$  of metal oxide samples

Sample	$S_{\text{BET}} / \text{m}^2 \text{g}^{-1}$	$N_s / 10^{-5} \text{mol m}^{-2}$	Method
$\text{Al}_2\text{O}_3$ (ALO-4)	155	3.20	Grignard
$\text{Cr}_2\text{O}_3$ (Kanto)	1.09	2.69	Grignard
$\text{Fe}_2\text{O}_3$ (Kanto A)	15.9	2.38	NaOH
$\text{Fe}_2\text{O}_3$ (Kanto B)	5.60	2.36	Grignard
$\text{Fe}_3\text{O}_4$ (Kanto)	4.32	3.31	Grignard
$\text{Fe}_3\text{O}_4$ (Sphere)	1.73	1.08	NaOH
$\text{MnO}_2$ (IC1)	43.0	2.25	Grignard
$\text{MnO}_2$ (IC12)	80.0	2.35	Grignard
$\text{MnO}_2$ (IC22)	45.1	2.41	Grignard
$\text{SiO}_2$ (SIO-1)	92.6	1.60	Grignard
$\text{SiO}_2$ (Kanto)	245	0.954	Grignard
$\text{TiO}_2$ (TIO-5)	2.60	1.80	Grignard
$\text{TiO}_2$ (Kanto)	21.5	1.16	Grignard

ALO-4, SIO-1, TIO-5: Reference Catalyst, supplied from the Catalysis Society of Japan. Kanto: Kanto Chemical CO., Tokyo, Japan. IC1, 12, 22: International Common Samples for batteries, supplied from the IC Sample Office, Cleveland, OH, USA. Sphere: Synthesized spherical particles. (Ref. 28)

**Table 2** Values of equilibrium and interaction constants of ion-site pairs for metal oxide samples at ionic strength 0.1 M ( $\text{NaNO}_3$ ) and 25°C

Sample	$\log K_a^o$	$\log K_b^o$	$\log A_a$	$\log A_b$	PZC
$\text{MnO}_2$ (IC 1)	-3.98	-9.95	1.35	0.96	4.15
$\text{MnO}_2$ (IC 12)	-4.25	-10.9	1.47	0.91	3.76
$\text{MnO}_2$ (IC 22)	-5.11	-9.89	1.57	0.99	4.72
$\text{TiO}_2$ (TIO-5)	-6.10	-9.20	1.39	1.63	5.36
$\text{Fe}_2\text{O}_3$ (Kanto B)	-5.95	-9.13	1.49	1.45	5.34
$\text{Fe}_3\text{O}_4$ (Kanto)	-6.66	-8.04	1.65	1.76	6.25
$\text{Al}_2\text{O}_3$ (ALO-4)	-9.25	-6.05	1.31	1.90	8.44

(Ref. 28)

**Table 3** Values of equilibrium and interaction constants of alkali metal ion-site pairs for MnO<sub>2</sub> (IC12) at ionic strength 0.1 M and 25°C

Ion	$\log K_a^o$	$\log A_a$
Li <sup>+</sup>	-4.50	1.29
Na <sup>+</sup>	-4.25	1.47
K <sup>+</sup>	-3.40	1.65
Cs <sup>+</sup>	-3.20	1.71

(Ref. 47)

**Table 4** Values of equilibrium and interaction constants of Co(II) surface complexes for metal oxides at ionic strength 0.1 M ( $\text{NaNO}_3$ ) and 25°C

Surface complex	$\log K_1^\circ$	$\log \beta_2^\circ$	$\log B_1$	$\log B_2$
$\text{Co}^{2+}\text{-MnO}_2$ (IC12)	-4.32	2.48	1.08	1.67
$\text{Co}^{2+}\text{-Fe}_3\text{O}_4$ (Sphere)	-4.98	-1.02	0.80	1.47
$\text{Co}^{2+}\text{-TiO}_2$ (Kanto)	-5.53	-0.91	0.94	2.26
$\text{Co}^{2+}\text{-Fe}_2\text{O}_3$ (Kanto A)	-6.32	-0.75	1.62	2.23
$\text{Co}^{2+}\text{-Al}_2\text{O}_3$ (ALO-4)	-6.62	-3.02	1.88	2.47

$K_1^\circ$  ( $\text{mol}^{-1} \text{m}^3$ ),  $\beta_2^\circ$  ( $\text{m}^{-1}$ )

(Ref. 48)

**Table 5** Values of equilibrium and interaction constants of M( II ) surface complexes for MnO<sub>2</sub> and Fe<sub>2</sub>O<sub>3</sub> at ionic strength 0.1 M (NaNO<sub>3</sub>) and 25°C

Surface complex	log $K_1^o$	log $\beta_2^o$	log $B_1$	log $B_2$
Ni <sup>2+</sup> -MnO <sub>2</sub> (IC12)	-4.43	2.31	1.20	1.98
Zn <sup>2+</sup> -Fe <sub>3</sub> O <sub>4</sub> (IC12)	-3.91	1.84	1.25	1.89
Co <sup>2+</sup> -MnO <sub>2</sub> (IC12)	-4.32	2.48	1.08	1.67
Mn <sup>2+</sup> - MnO <sub>2</sub> (IC12)	-1.99	2.61	1.88	0.80
Cu <sup>2+</sup> - MnO <sub>2</sub> (IC12)	-2.09	3.38	1.65	0.98
Co <sup>2+</sup> -Fe <sub>2</sub> O <sub>3</sub> (Kanto A)	-6.32	-0.75	1.62	2.23
Zn <sup>2+</sup> -Fe <sub>2</sub> O <sub>3</sub> (Kanto A)	-6.07	-0.610	1.75	2.81
Cu <sup>2+</sup> -Fe <sub>2</sub> O <sub>3</sub> (Kanto A)	-4.28	0.00	2.16	0.92
Pb <sup>2+</sup> -Fe <sub>2</sub> O <sub>3</sub> (Kanto A)	-3.70	1.40	1.78	1.70

$K_1^o$  (mol<sup>-1</sup> m<sup>3</sup>),  $\beta_2^o$ (m<sup>-1</sup>)

(Ref. 49)

**Table 6** Values of equilibrium and interaction constants of alkali metal ion( $M^+$ )-site pairs for Amberlite IRC-84 at ionic strength 0.5 M ( $MNO_3$ ) and 25°C

$M^+$	$\log K_{w\text{-nano}}^o$	$\log K_{n\text{-nano}}^o$	$\log A_{w\text{-nano}}$	$\log A_{n\text{-nano}}$	$\phi_{w\text{-nano}}$
$Li^+$	-3.09	-4.75	1.09	0	0.285
$Na^+$	-3.39	-4.78	0.987	0.103	0.509
$K^+$	-3.26	-5.16	0.992	0.274	0.497
$Cs^+$	-3.34	-5.35	1.07	0.306	0.461

**Table 7** Values of equilibrium and interaction constants of alkali metal ion( $M^+$ )-site pairs for Amberlite IRC-50 at ionic strength 0.5 M  $MNO_3$  and 25°C

$M^+$	$\log K_{\text{macro}}^o$	$\log K_{\text{w-nano}}^o$	$\log A_{\text{macro}}$	$\log A_{\text{w-nano}}$	$\phi_{\text{macro}}$
$Li^+$	-5.37	-5.59	0.16	1.08	0.74
$Na^+$	-5.42	-5.85	0.35	1.08	0.73
$K^+$	-5.55	-6.50	0.33	1.11	0.73
$Cs^+$	-5.81	-5.62	0.36	1.19	0.68

Figure 1

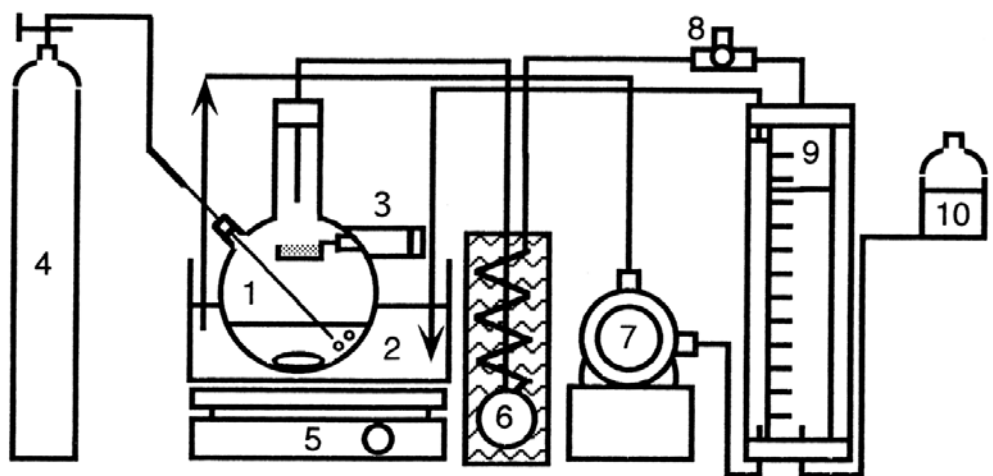


Figure 2

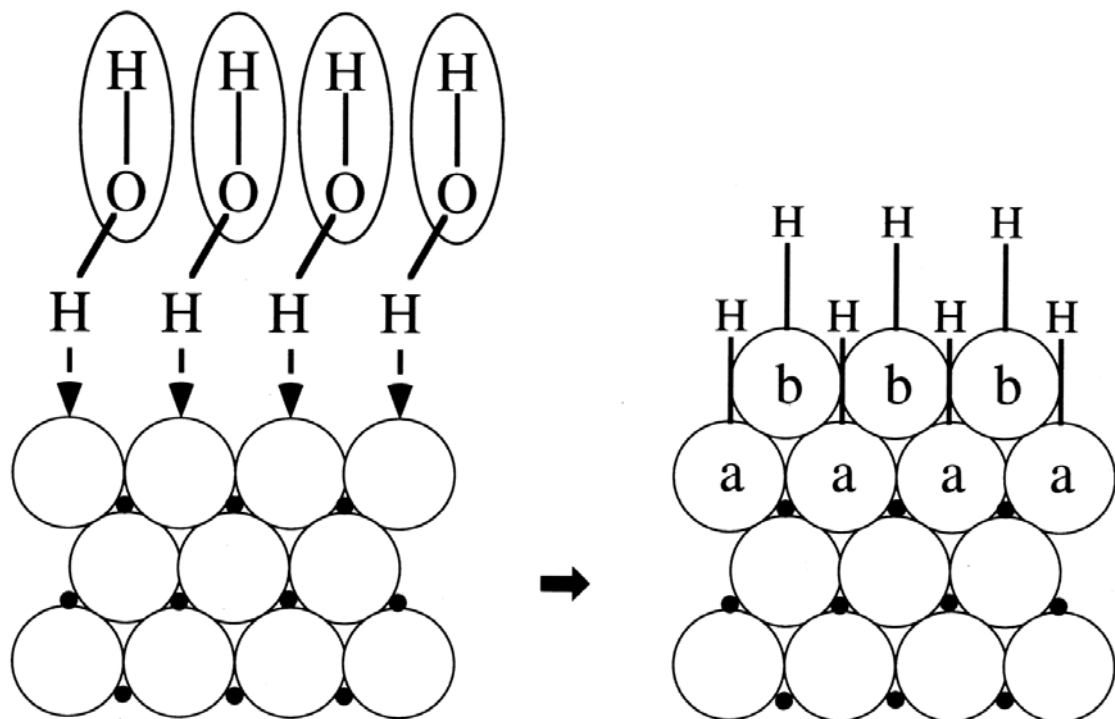


Figure 3

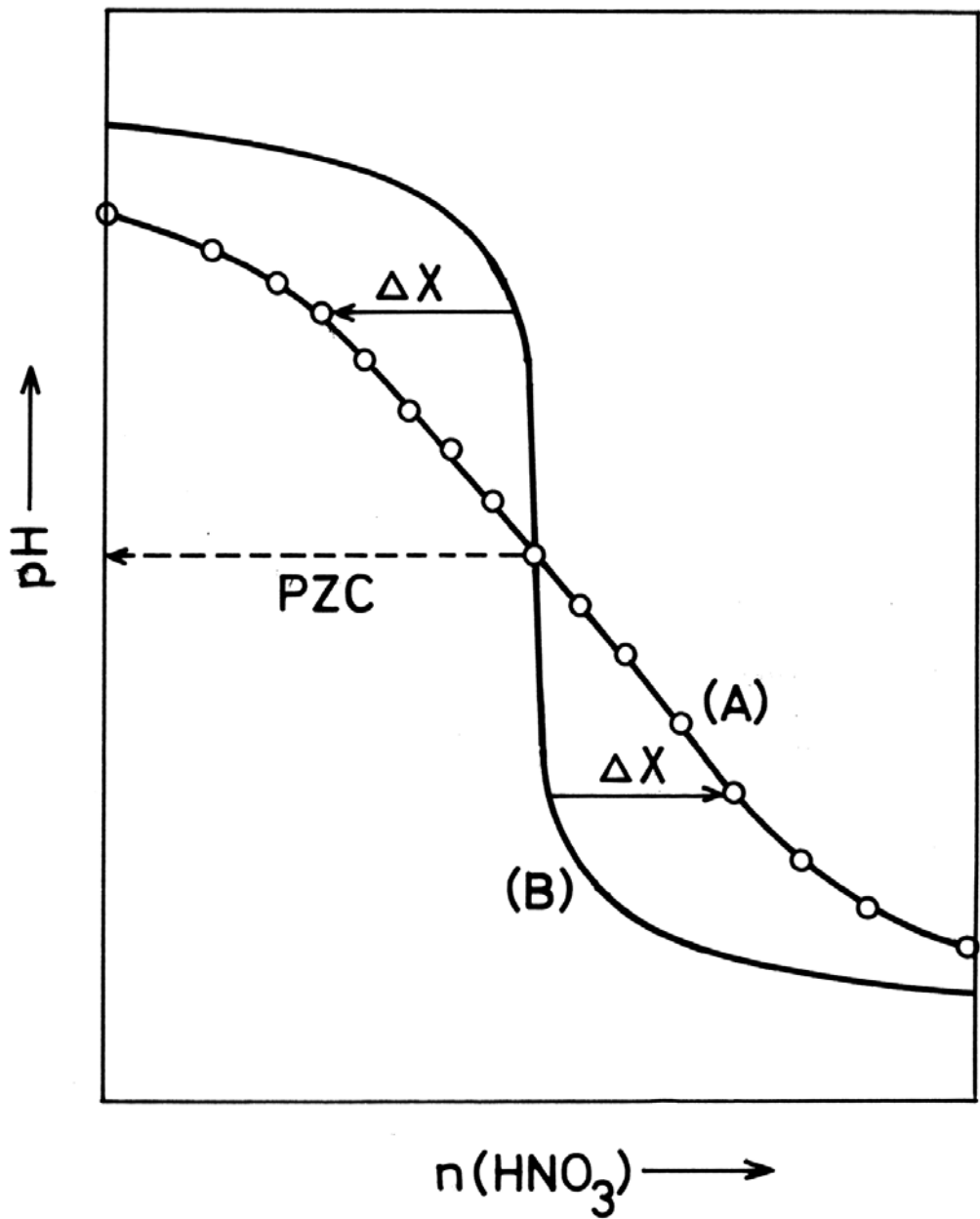


Figure 4

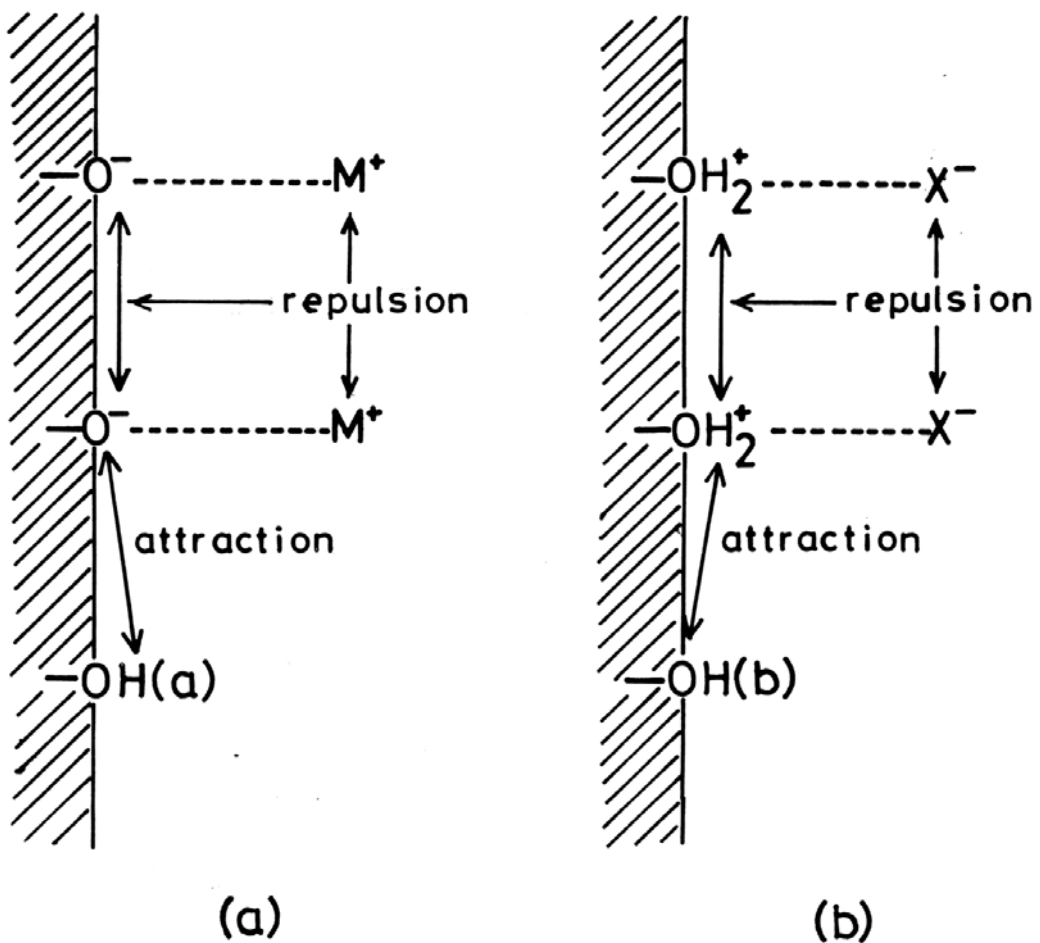


Figure 5

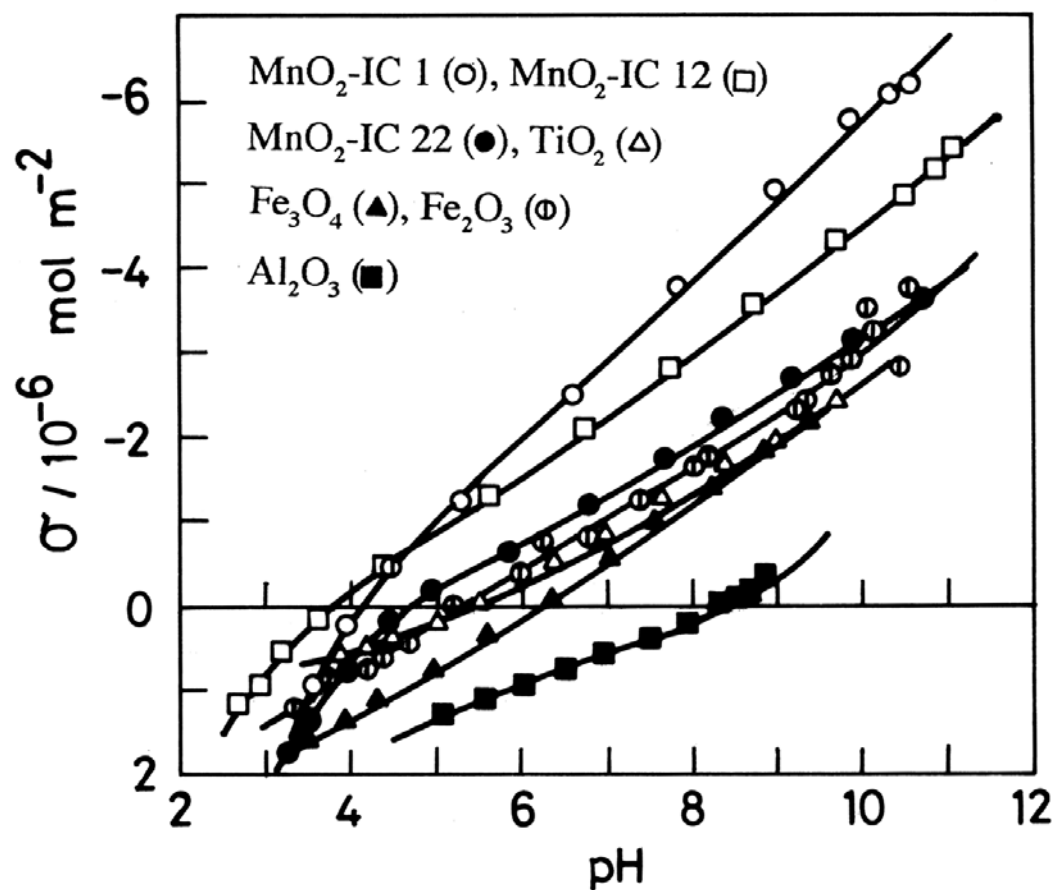


Figure 6

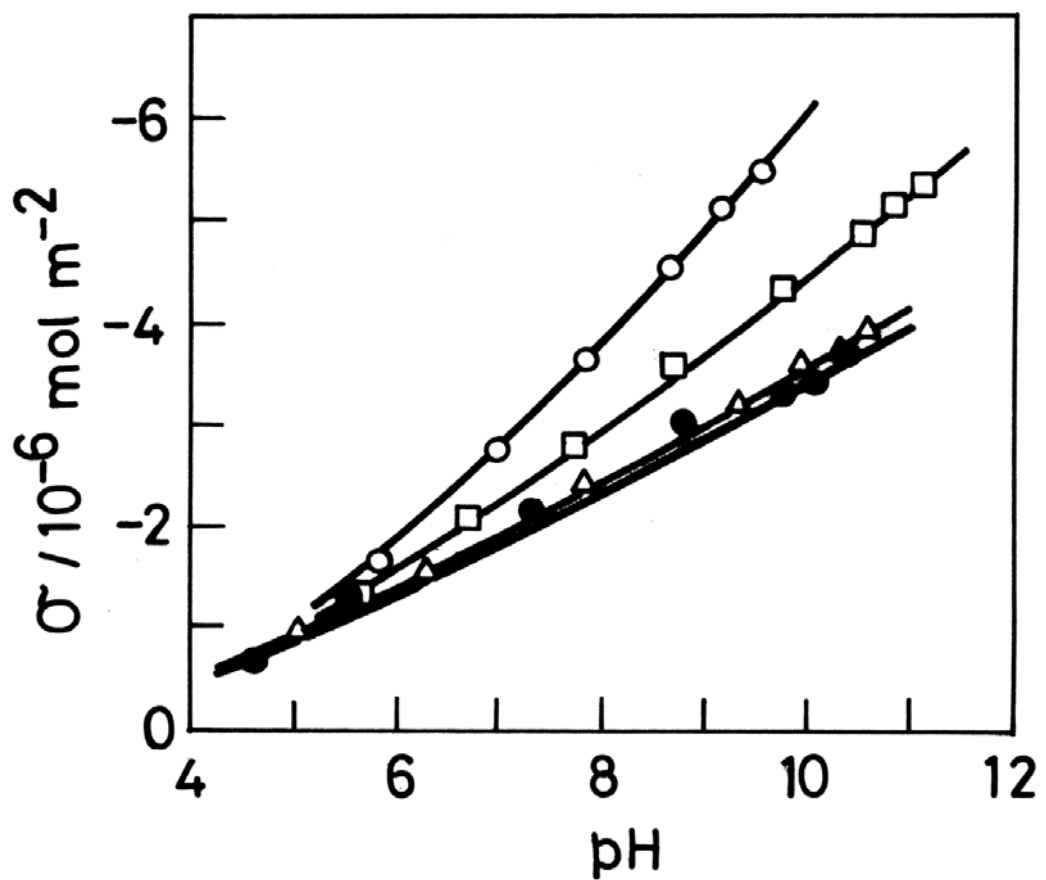


Figure 7

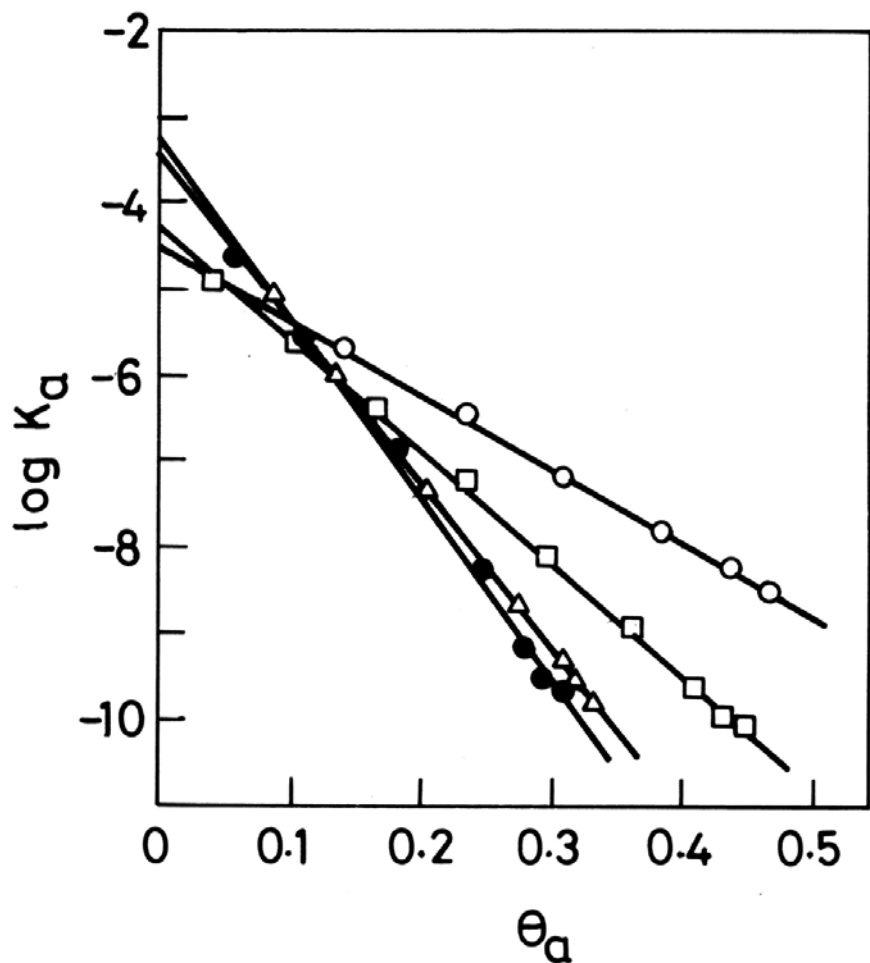


Figure 8

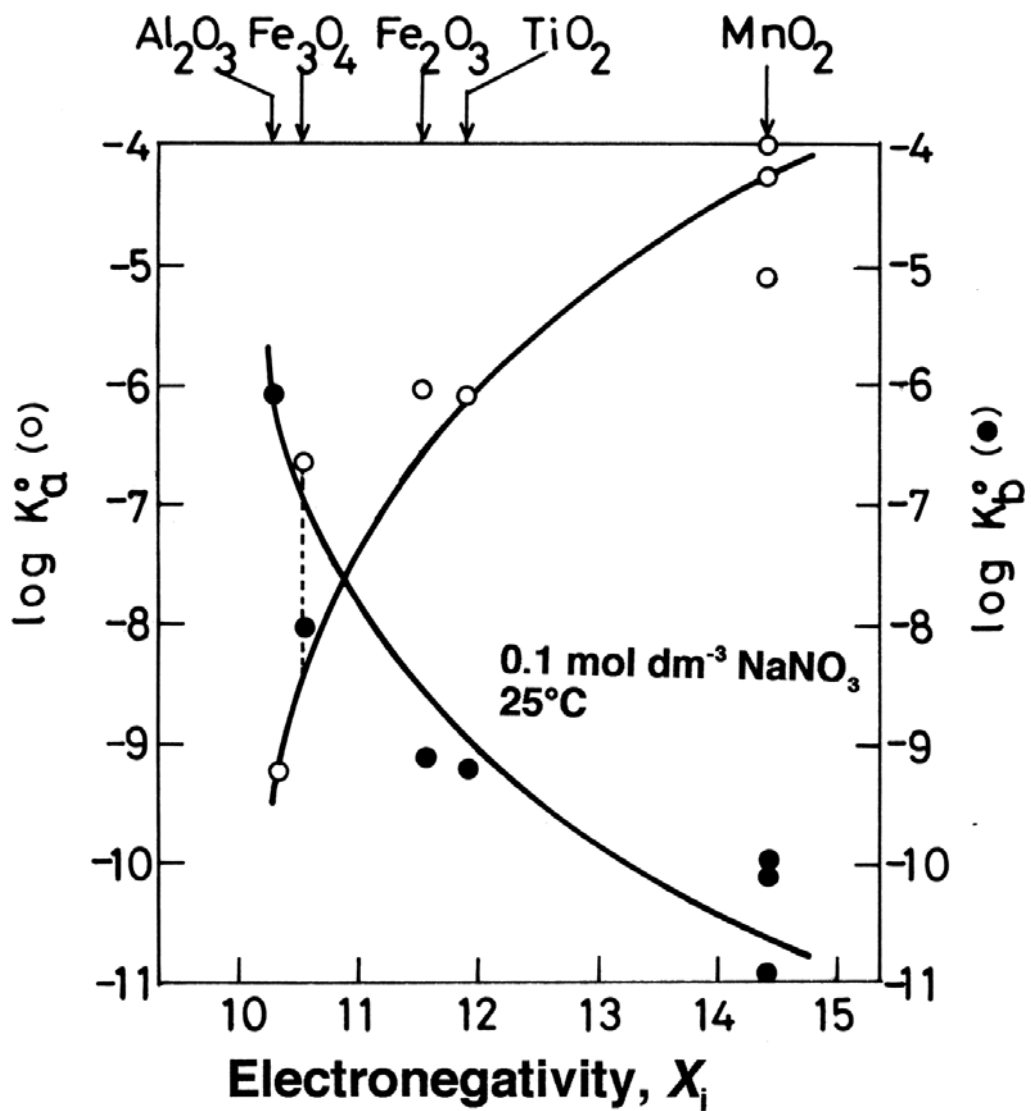


Figure 9

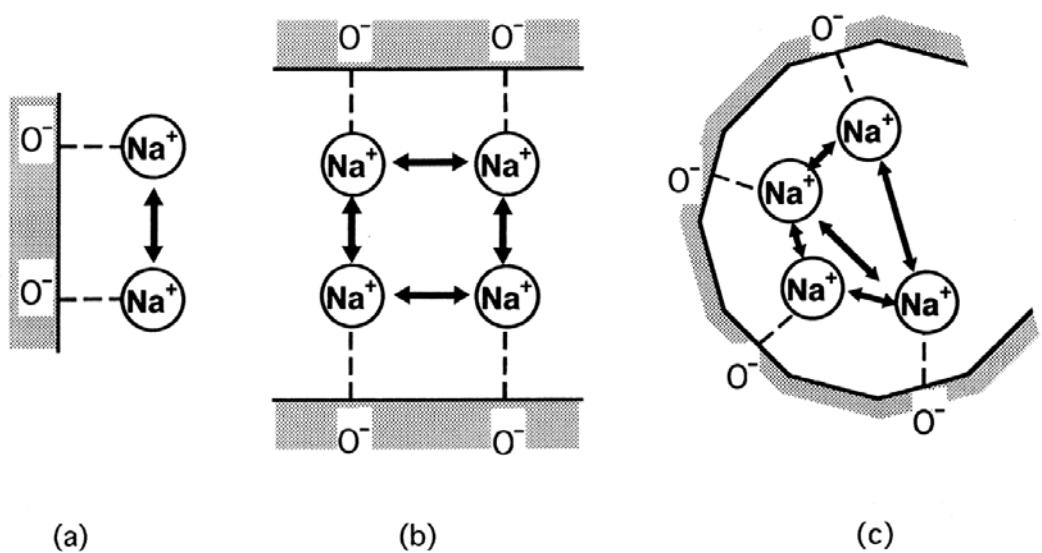


Figure 10

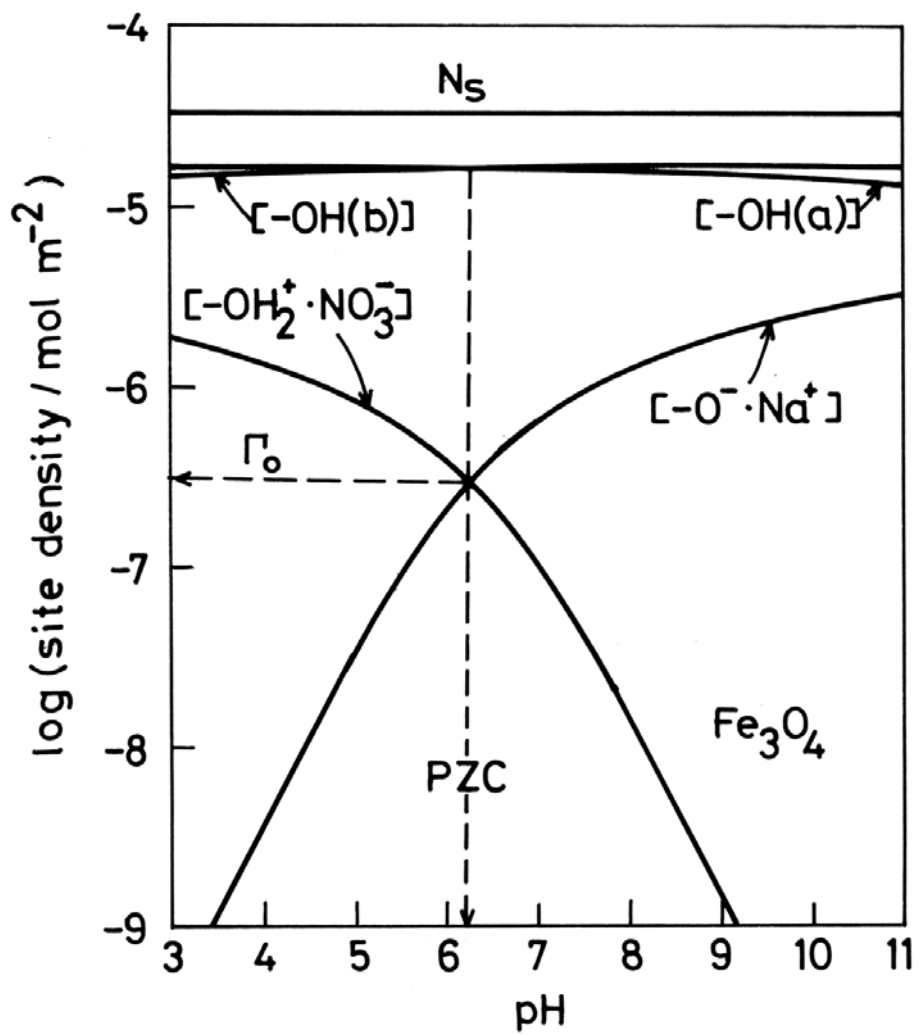


Figure 11

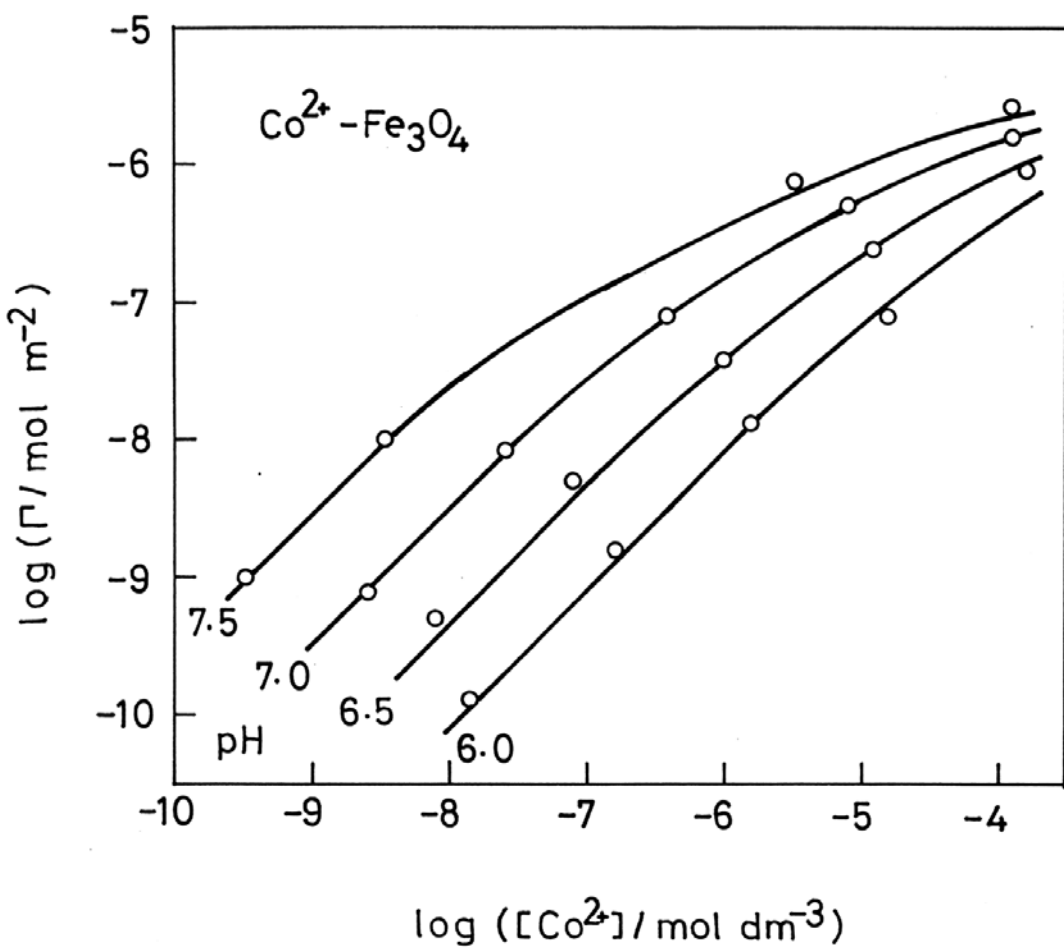


Figure 12

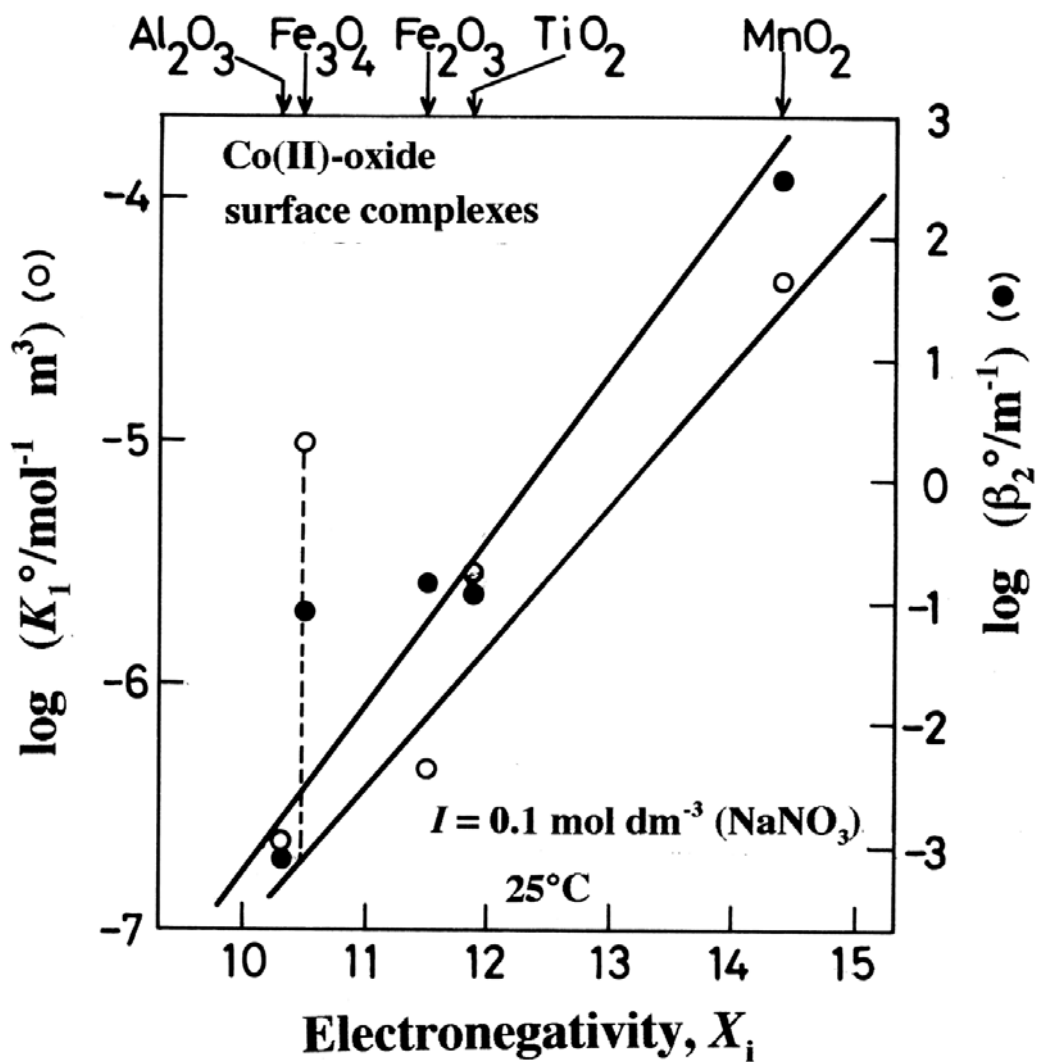


Figure 13

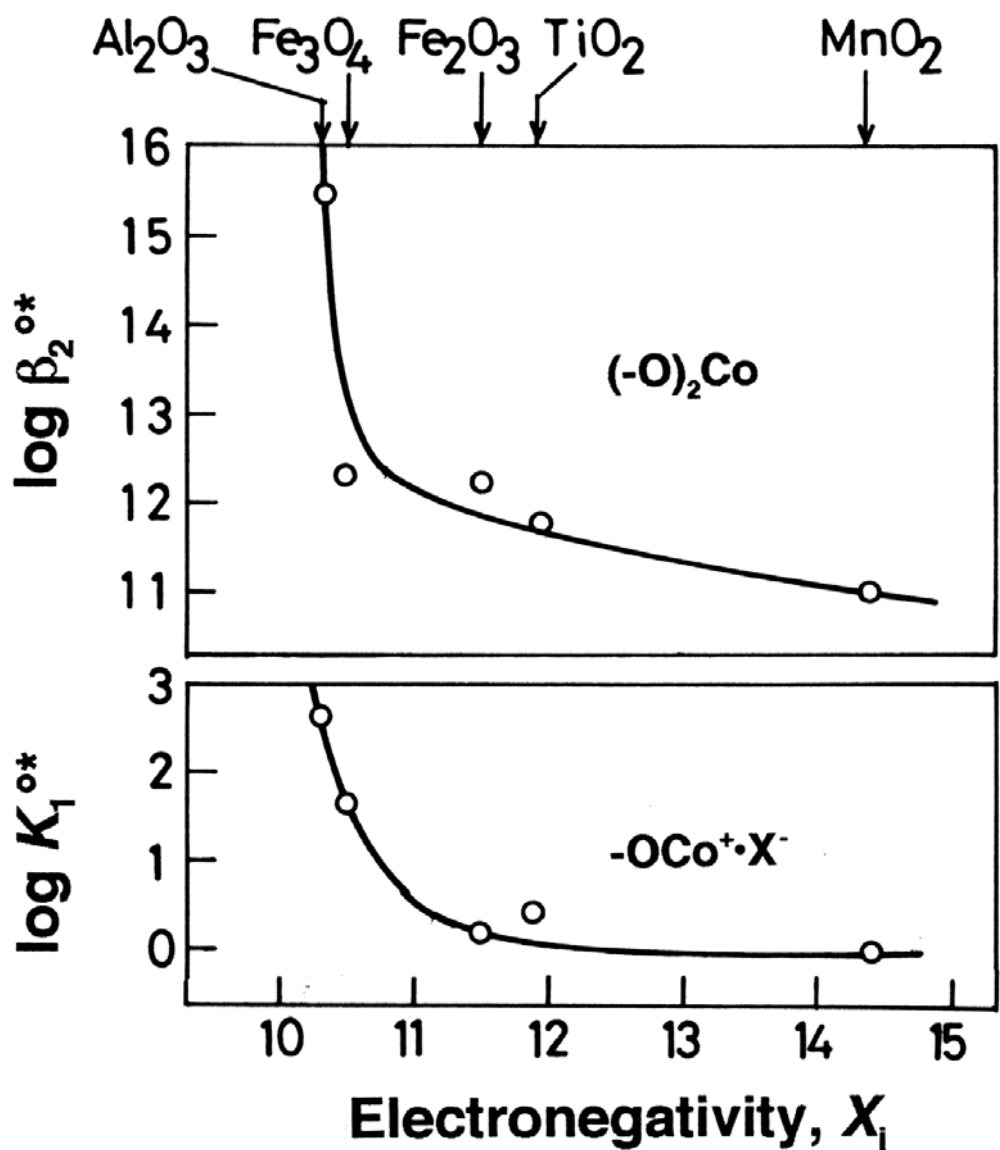


Figure 14

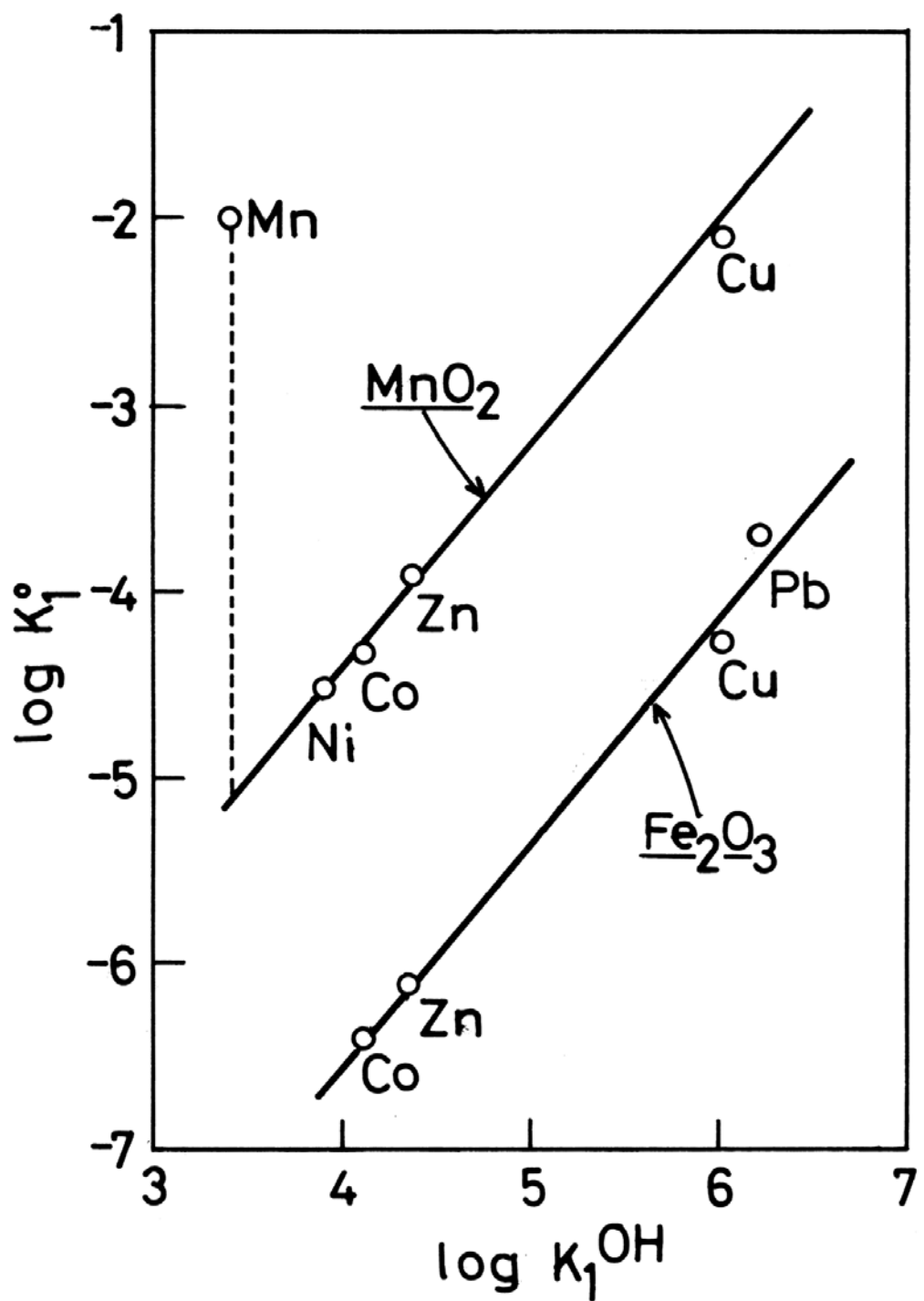


Figure 15

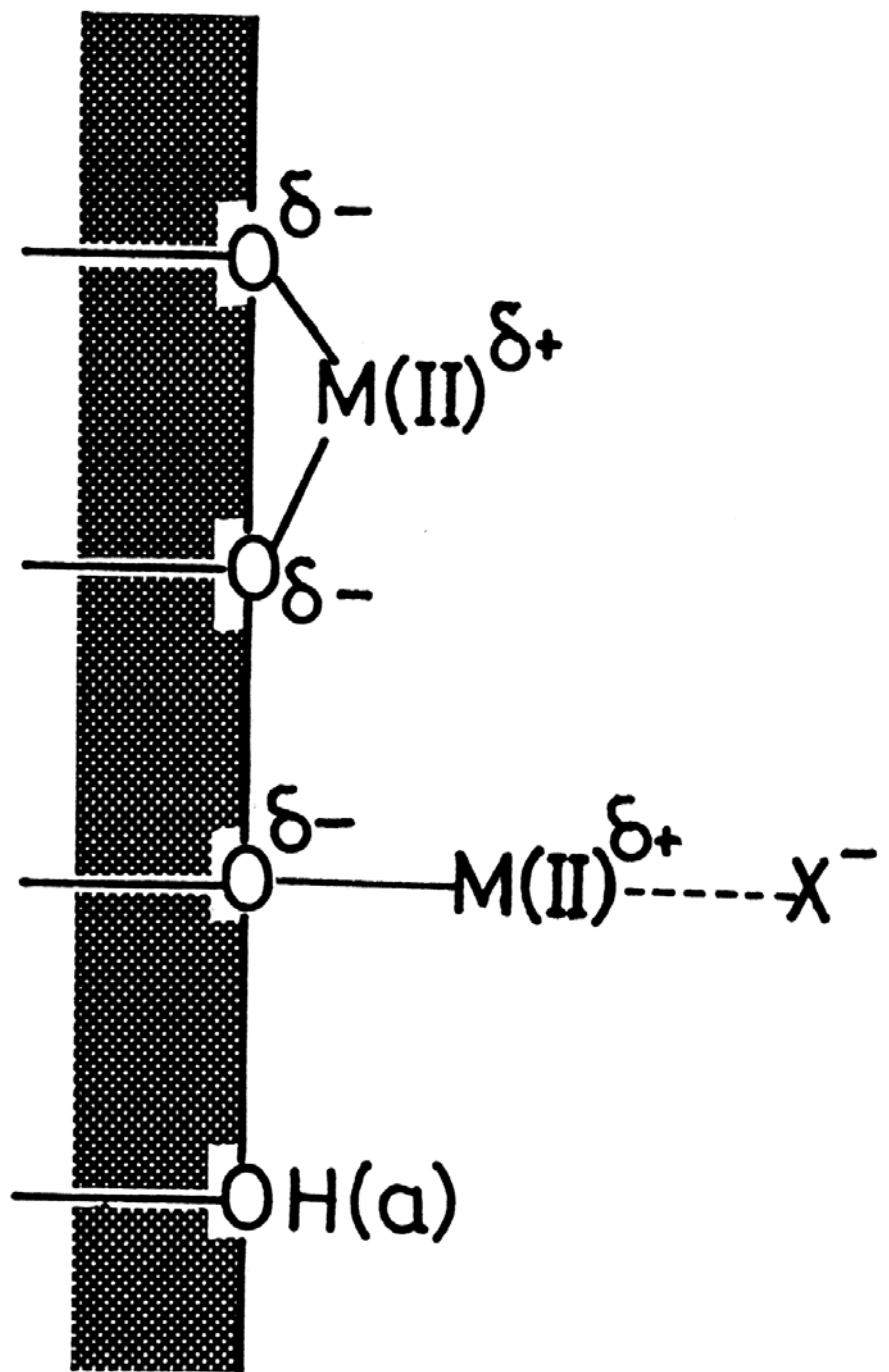


Figure 16

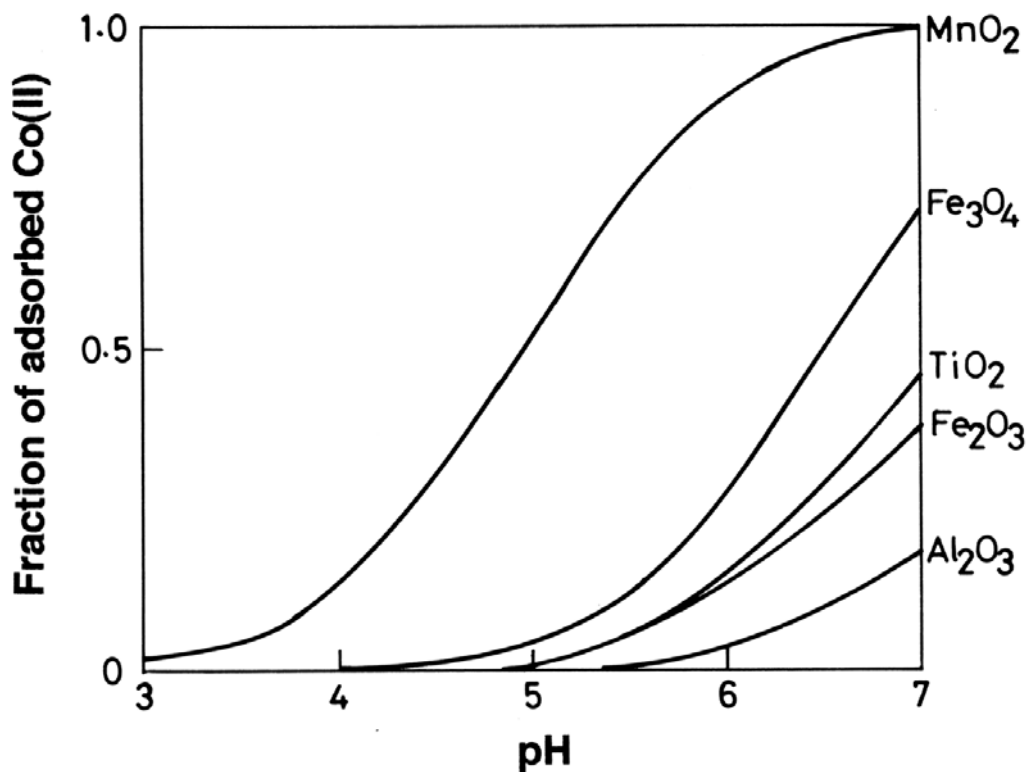


Figure 17

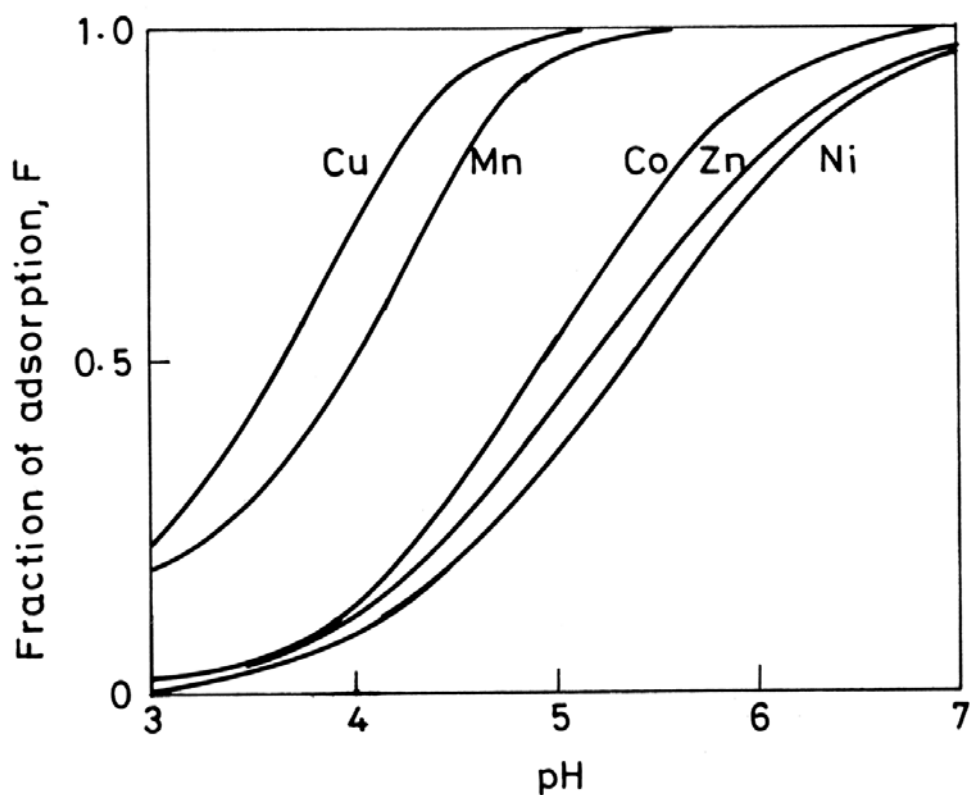


Figure 18

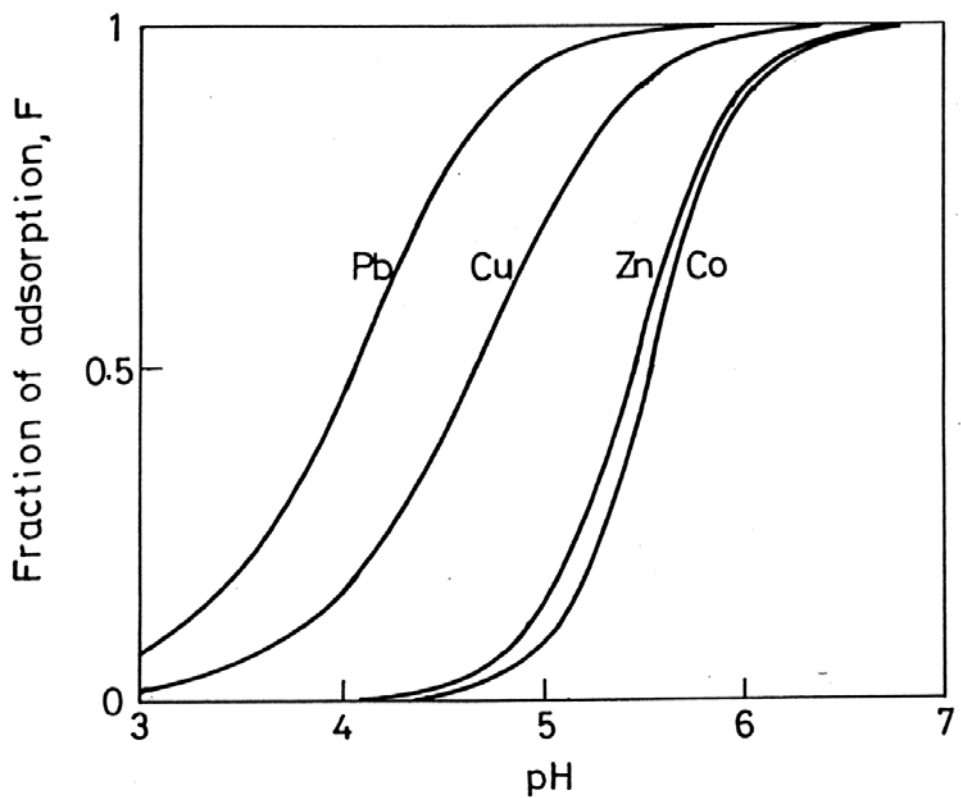


Figure 19

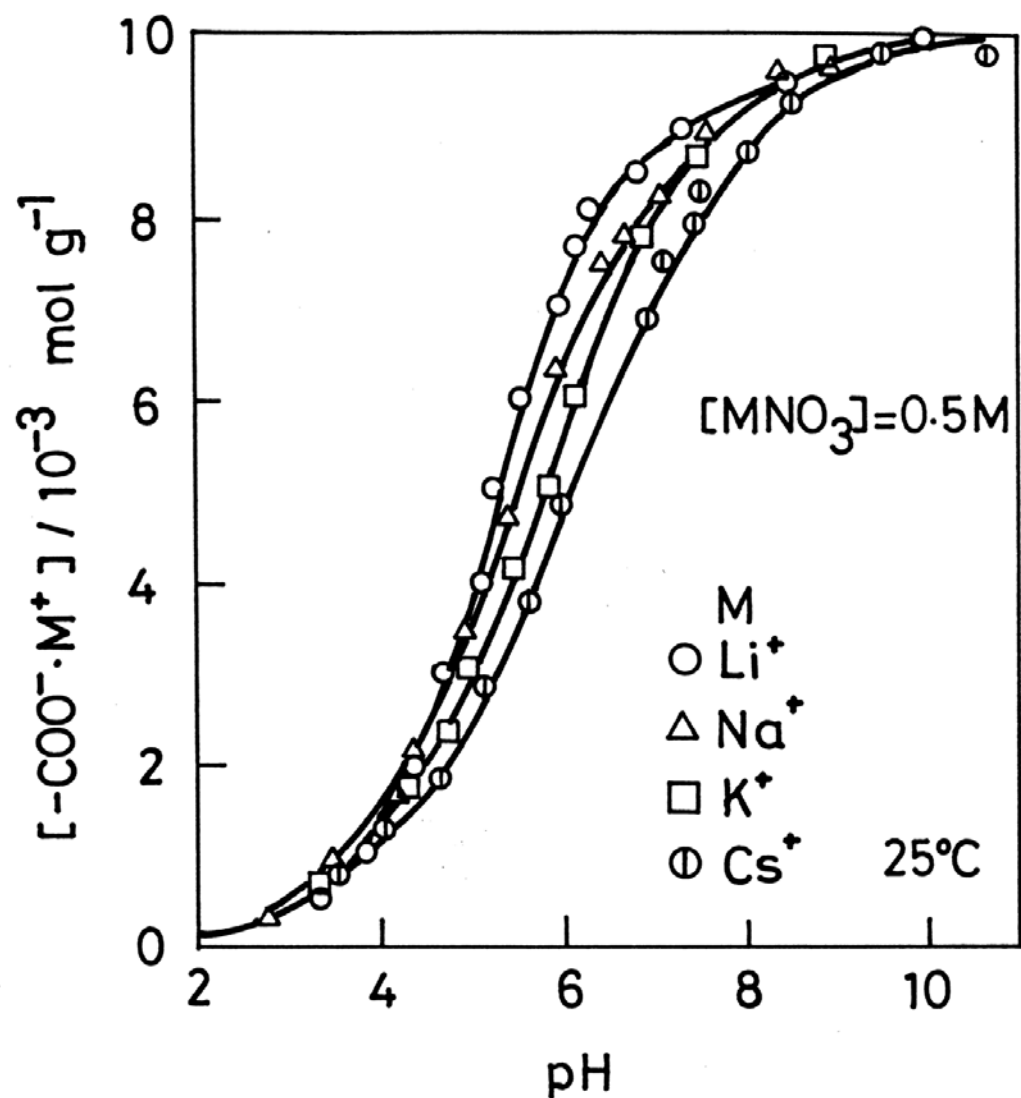
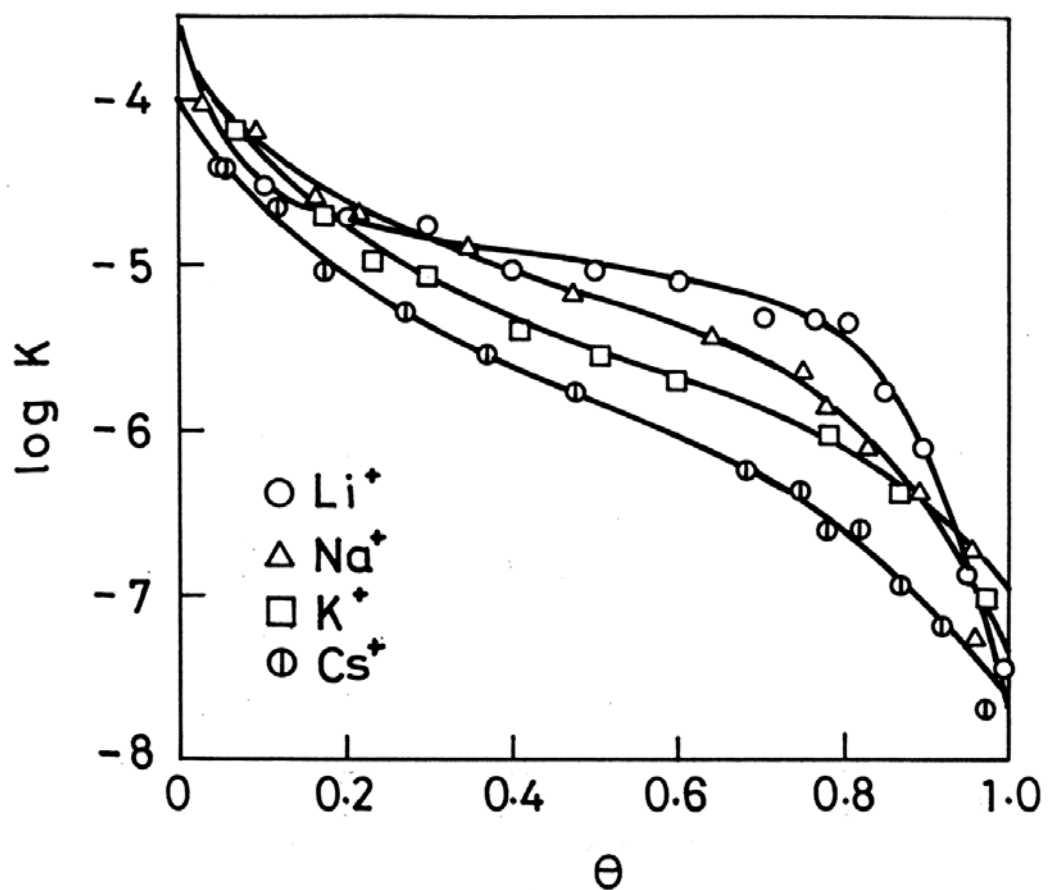


Figure 20



**Figure 21**

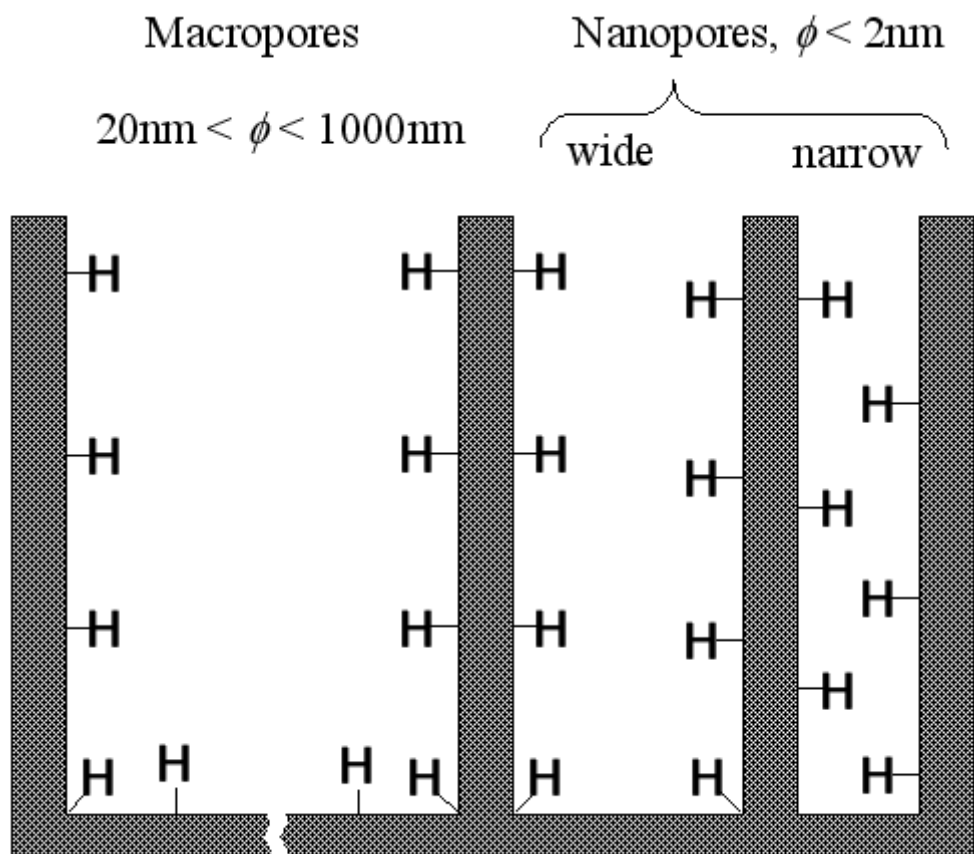


Figure 22

